Monthly Notices
of the
ROYAL ASTRONOMICAL SOCIETY

MNRAS **457,** 82–109 (2016) doi:10.1093/mnras/stv2972

A very deep *Chandra* view of metals, sloshing and feedback in the Centaurus cluster of galaxies

J. S. Sanders,[1]★ A. C. Fabian,[2] G. B. Taylor,[3] H. R. Russell,[2] K. M. Blundell,[4] R. E. A. Canning,[5,6] J. Hlavacek-Larrondo,[7,5,6] S. A. Walker[2] and C. K. Grimes[3]

[1] *Max-Planck-Institut für extraterrestrische Physik, Giessenbachstrasse 1, D-85748 Garching, Germany*
[2] *Institute of Astronomy, Madingley Road, Cambridge CB3 0FT, UK*
[3] *Department of Physics and Astronomy, University of New Mexico, Albuquerque, NM 87131, USA*
[4] *University of Oxford, Astrophysics, Keble Road, Oxford OX1 3RH, UK*
[5] *Kavli Institute for Particle Astrophysics and Cosmology, Stanford University, 452 Lomita Mall, Stanford, CA 94305, USA*
[6] *Department of Physics, Stanford University, 382 Via Pueblo Mall, Stanford, CA 94305, USA*
[7] *Département de Physique, Université de Montréal, C.P. 6128, Succ. Centre-Ville, Montreal, QC H3C 3J7, Canada*

Accepted 2015 December 18. Received 2015 November 26; in original form 2015 August 11

ABSTRACT

We examine deep *Chandra* X-ray observations of the Centaurus cluster of galaxies, Abell 3526. Applying a gradient magnitude filter reveals a wealth of structure, from filamentary soft emission on 100 pc (0.5 arcsec) scales close to the nucleus to features 10 s of kpc in size at larger radii. The cluster contains multiple high-metallicity regions with sharp edges. Relative to an azimuthal average, the deviations of metallicity and surface brightness are correlated, and the temperature is inversely correlated, as expected if the larger scale asymmetries in the cluster are dominated by sloshing motions. Around the western cold front are a series of ∼7 kpc ‘notches’, suggestive of Kelvin–Helmholtz instabilities. The cold front width varies from 4 kpc down to close to the electron mean free path. Inside the front are multiple metallicity blobs on scales of 5–10 kpc, which could have been uplifted by AGN activity, also explaining the central metallicity drop and flat inner metallicity profile. Close to the nucleus are multiple shocks, including a 1.9-kpc-radius inner shell-like structure and a weak 1.1–1.4 Mach number shock around the central cavities. Within a 10 kpc radius are nine depressions in surface brightness, several of which appear to be associated with radio emission. The shocks and cavities imply that the nucleus has been repeatedly active on 5–10 Myr time-scales, indicating a tight balance between heating and cooling. We confirm the presence of a series of linear quasi-periodic structures. If they are sound waves, the ∼5 kpc spacing implies a period of 6 Myr, similar to the ages of the shocks and cavities. Alternatively, these structures may be Kelvin–Helmholtz instabilities, their associated turbulence or amplified magnetic field layers.

Key words: galaxies: clusters: individual: Abell 3526 – X-rays: galaxies: clusters.

1 INTRODUCTION

The Centaurus cluster, Abell 3526, is one of the X-ray brightest and nearest galaxy clusters in the sky, with a flux of $2.7 \times 10^{-10}\,\mathrm{erg\,cm^{-2}\,s^{-1}}$ in the 0.1 to 2.4 keV band, corresponding to a bolometric luminosity of $1.1 \times 10^{44}\,\mathrm{erg\,s^{-1}}$ (Reiprich & Böhringer 2002). The cluster has two sub-components, a main cluster Cen 30, with a redshift of 0.0104 and a subcluster, Cen 45, 15 arcmin (∼200 kpc) to the east with a velocity $1500\,\mathrm{km\,s^{-1}}$ higher (Lucey, Currie & Dickens 1986).

The first *Chandra* observations (Sanders & Fabian 2002) of the cluster revealed a plume-like soft X-ray structure extending from the nucleus and multiphase X-ray material on small spatial scales. Deeper *Chandra* observations (Fabian et al. 2005) showed that the central region contains multiple inner cavities, where the radio plasma displaces the X-ray emitting material (Taylor, Fabian & Allen 2002). The plume was resolved into wispy filaments of soft, cool, X-ray emitting gas. The data also showed two semicircular edges in surface brightness (SB) to the east and west, where the temperature also changes, likely to be cold fronts (Markevitch & Vikhlinin 2007), discontinuities where the temperature and density change but the gas is in pressure equilibrium. Comparison with simulations indicates that the gas is sloshing about in the potential well.

★ E-mail: jsanders@mpe.mpg.de

Published by Oxford University Press on behalf of the Royal Astronomical Society

XMM–Newton Reflection Grating Spectrometer (RGS) observations (Sanders et al. 2008) of the cluster core revealed a spectrum with emission from Fe XVII to XXIV, but not O VII, showing there is X-ray emitting material down to temperatures between 0.3 and 0.45 keV. Above 2 keV the spectra are consistent with 40 $\mathrm{M}_{\odot}\ \mathrm{yr}^{-1}$ of radiative cooling, but at 1 keV this reduces to 4 $\mathrm{M}_{\odot}\ \mathrm{yr}^{-1}$ and less than 0.8 $\mathrm{M}_{\odot}\ \mathrm{yr}^{-1}$ appears to be cooling below 0.4 keV. From the outskirts to the centre, the temperature of the intracluster medium (ICM) decreases by a factor of ∼10. The mean radiative cooling time of the ICM drops to $\sim 10^{7}$ yr in the centre.

The soft X-ray emission in the core of the cluster is correlated with atomic and molecular material at much lower temperatures. The central galaxy, NGC 4696, contains a dust lane (Shobbrook 1963) and has bright filamentary central Hα emission (Fabian et al. 1982), both of which have similar morphologies (Sparks, Macchetto & Golombek 1989). These components are themselves correlated with the cool X-ray emitting filaments (Crawford et al. 2005), and appear to be drawn up by buoyant bubbles rising in the ICM (Crawford et al. 2005). This model is supported by deep integral-field spectroscopy (Canning et al. 2011b), who find no evidence for fast shock excitation and whose spectra support the particle heating excitation model of Ferland et al. (2009).

Using *Spitzer*, Johnstone et al. (2007) found evidence for pure-rotational lines from molecular hydrogen, indicating an excitation temperature of 300–400 K. The flux in the 0−0 S(1) molecular hydrogen line correlates well with the strength of the optical lines. Molecular material cooler than 400 K dominates the mass of the outer filaments. With *Herschel*, Mittal et al. (2011) found two of the strongest cooling lines in the interstellar medium, [C II] and [O I]. The [C II] emission has a similar morphology and velocity structure compared to the Hα emission, suggesting that the soft X-rays, optical lines and far-infrared have the same energy source. In addition *Herschel* found $1.6 \times 10^{6}\ \mathrm{M}_{\odot}$ of dust at 19 K, although the FIR luminosity suggests a low 0.13 $\mathrm{M}_{\odot}\ \mathrm{yr}^{-1}$ star formation rate.

Canning et al. (2011a) detected optical coronal emission from 10^{6} K gas in the core of the cluster. The lowest temperature probe [Fe X] λ6374 is twice as bright as expected. Chatzikos et al. (2015) suggest that the coronal spectrum is not indicative of cooling material, but instead comes from a conductive or mixing interface between the X-ray plume and optical filaments.

The *Chandra* observations confirmed that the cluster has a high (1.5-2 $\mathrm{Z}_{\odot}$) metallicity flat core with a sharp edge, previously seen using *ROSAT* and *ASCA* data (Allen & Fabian 1994; Fukazawa et al. 1994; Ikebe et al. 1999; Allen et al. 2001). The boxy metallicity profile requires a large effective diffusion coefficient which drops very rapidly with radius (Graham et al. 2006). The metallicity ratios in the core of the cluster are roughly consistent with solar values (Sanders & Fabian 2006b), indicating enrichment by both Type Ia and II supernovae, although O and Mg are ∼40 per cent less abundant (Sakuma et al. 2011). The metallicity profile and ratios show that the centre of the cluster appears to have not suffered major disruption over the past 8 Gyr or longer.

In the centre of the cluster there is a drop in the observed metallicity (Sanders & Fabian 2002), which appears not to be caused by resonance scattering (Sanders & Fabian 2006a) or inadequate spectral modelling (Fabian et al. 2005). The decrement is consistent with the deposition of metals on to grains which are incorporated into dusty filaments (Panagoulia, Sanders & Fabian 2015).

The Cen 45 subcluster has a temperature excess surrounding it, interpreted as having been heated by its interaction with Cen 30 (Churazov et al. 1999). This excess was confirmed using *XMM* and can be explained by a simple shock heating model (Walker, Fabian & Sanders 2013). A pressure jump is also seen in the direction of the merger and the merging subcluster appears to have retained its metals. No bulk velocities greater than 1400 $\mathrm{km\,s}^{-1}$ in the ICM were detected in the cluster (Ota et al. 2007).

The extended component of the central radio source in the cluster, PKS 1246−410, appears to be interacting with and displacing the ICM (Taylor et al. 2002; Rudnick & Blundell 2003), most obviously seen by the presence of two central cavities in the ICM. The most extended radio emission appears to go beyond to regions of low thermal pressure, indicating there may be further X-ray cavities there (Crawford et al. 2005). The optical nucleus is double (Laine et al. 2003). The radio nucleus is associated with compact low-luminosity X-ray emission, but is offset from the X-ray-brightest region of the cluster (Taylor et al. 2006). If the nucleus were accreting at the Bondi rate, it would overproduce by 3.5 orders of magnitude its observed X-ray radiative luminosity. Very long baseline interferometry (VLBI) observations show a broad one-sided jet (Taylor et al. 2006). The cluster shows Faraday rotation measures (RMs), indicating magnetic fields of 25 μG on 1 kpc scales. The thermal pressure appears dominant over the magnetic pressure. The line-emitting gas, soft X-ray material, regions with an excess of RM and depolarized regions appear to be spatially correlated (Rudnick & Blundell 2003; Taylor et al. 2007).

Sanders & Fabian (2008) found X-ray SB ripples in several directions within the inner 40 kpc, postulating that they are sound waves in the ICM generated by the activity of the central nucleus, similar to those found in Perseus (Fabian et al. 2006) and Abell 2052 (Blanton et al. 2011). Such sound waves could transport energy from the nucleus to provide the distributed heating required to prevent the excepted high cooling rates.

In this paper, we present new results from 760 ks of *Chandra* observations, including 480 ks of new data. We assume the galaxy cluster lies at a redshift of 0.0104 (Lucey et al. 1986). Using $H_0 = 70\ \mathrm{km\,s}^{-1}\ \mathrm{Mpc}^{-1}$, 1 arcsec on the sky corresponds to 0.213 kpc. Images are aligned with north to the top and east to the left. For details of the data reduction, see Appendix A. We discuss the larger-scale structure in Section 2, including in detail sloshing gas in the potential well (Section 2.3), the western cold front (Section 2.4), the linear structures inside the cold front (Section 2.5) and the high-metallicity blobs (Section 2.6). In Section 3, we examine the inner region around the nucleus in detail, including the inner shock (Section 3.2), the interaction of the radio source and X-ray plasma (Section 3.3), the cavities (Section 3.4), the shock surrounding the cavities (Section 3.5), the association between soft X-rays and dust (Section 3.6), the origin of the plume (Section 3.7) and the RMs and magnetic fields (Section 3.8). We discuss the inner multiphase structure in Section 4 (also Appendix B), the central abundance drop in Section 5 and conclude in Section 6.

2 LARGER-SCALE STRUCTURE

2.1 X-ray images

Fig. 1 (top panel) is an X-ray image of the central 130 × 100 kpc of the cluster. There are 8.1×10^{6} counts in the data set inside a 5 arcmin radius. Prominent in the image is the central feedback region associated with NGC 4696, which we examine in depth in Section 3. There are SB edges, previously identified as cold fronts (Sanders & Fabian 2002; Fabian et al. 2005), 1.5 arcmin to the east and 3.3 arcmin to the west. We examine the western cold front in detail in Section 2.4. The depression 3.3 arcmin to the south-east

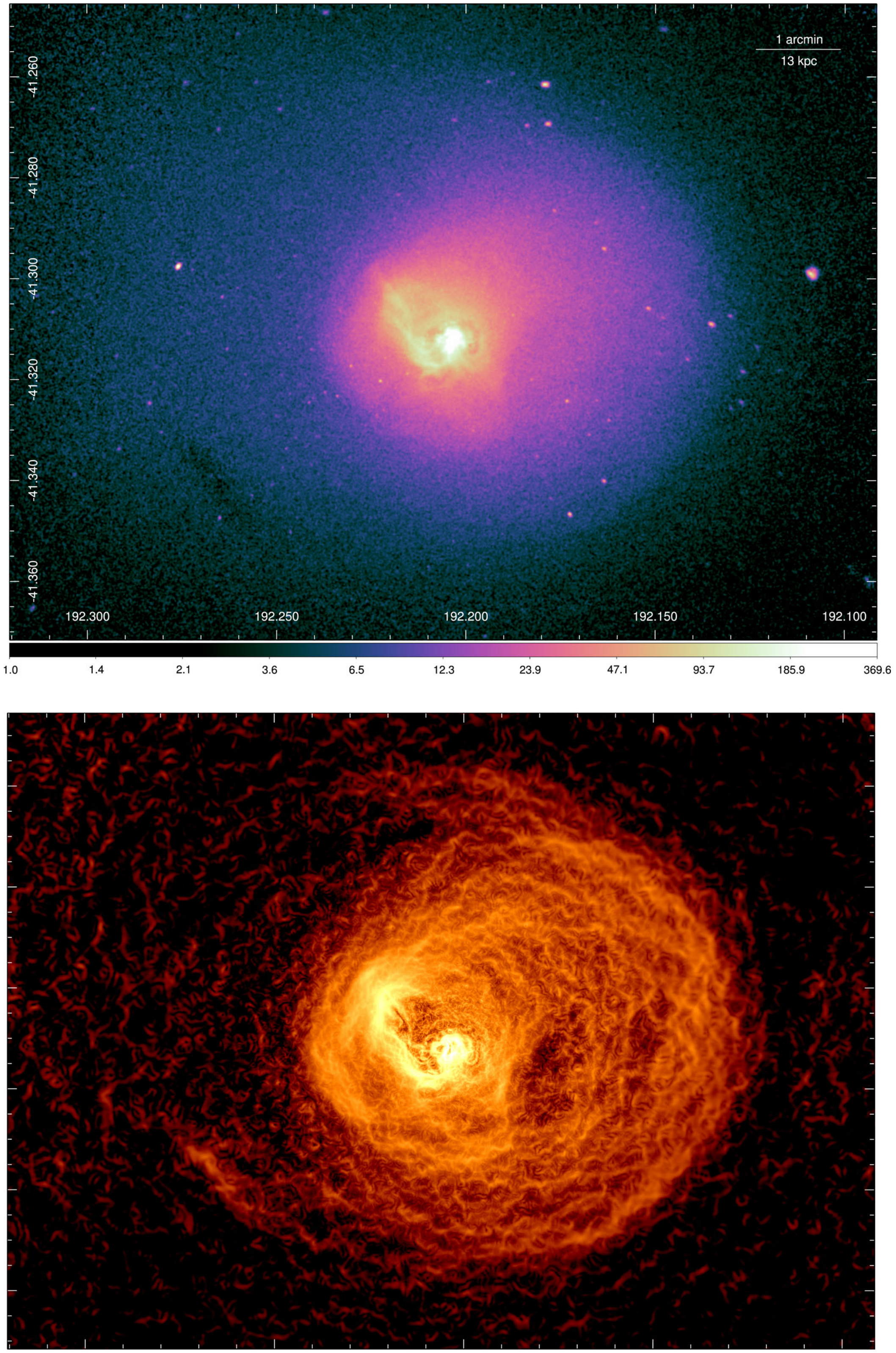

Figure 1. Top panel: X-ray image of the central 130 × 100 kpc of the cluster. The 0.5–7 keV image is background subtracted and exposure corrected. To the south-east can be seen the X-ray shadow of a disc galaxy. The colour bar shows the SB, scaled to show the central number of counts per 0.492 arcsec pixel. Bottom panel: the same region after applying GGM gradient filters with different scales and summing with radial scaling. Note that the scale is not consistent across the image and does not accurately reflect the magnitude of jumps. It emphasises the regions with largest SB gradients after point source removal.

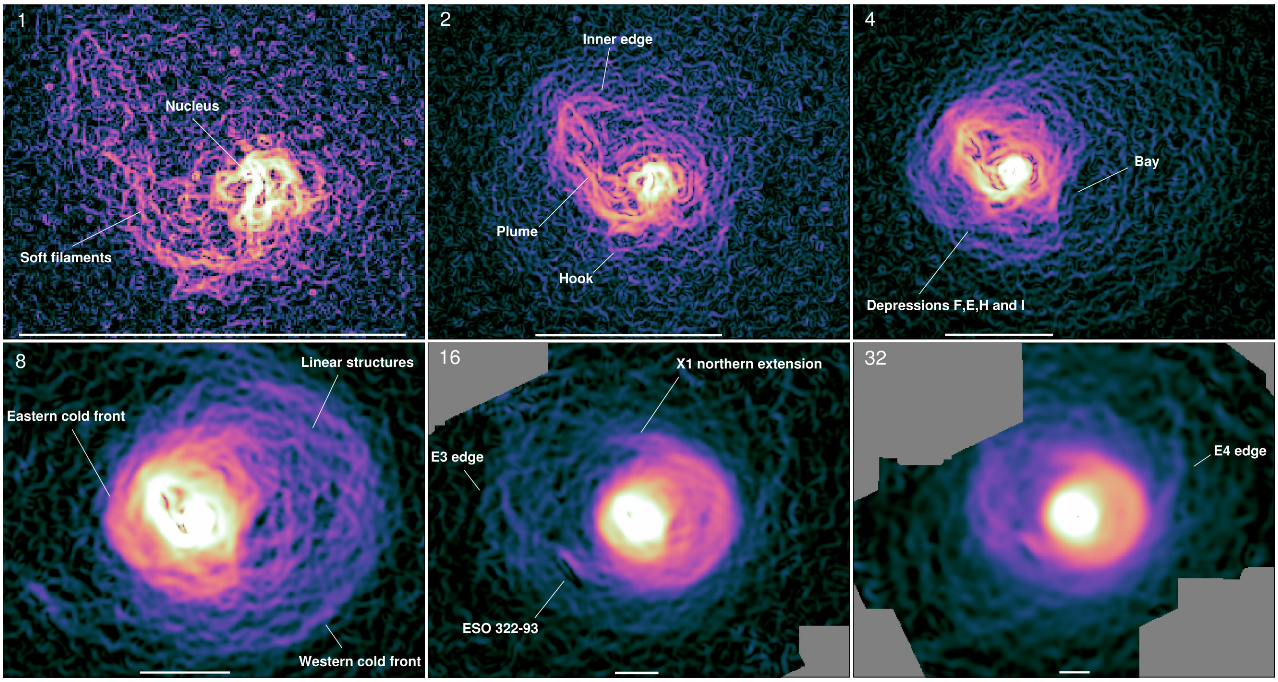

Figure 2. GGM gradient-filtered images using scales from 1 to 32 pixels (1 pixel is 0.492 arcsec). The white bar has a length of 20 kpc (∼94 arcsec). Labelled features are referred to in the text.

is due to an edge-on disc galaxy, ESO 322-93, in the main Cen 30 cluster which absorbs some soft cluster X-ray emission (Fabian et al. 2005).

To better examine the features in the image, we applied a gradient filter to highlight sharp and flat regions. Gradient filtering has previously been used to examine cluster simulations (Roediger et al. 2013). The Gaussian gradient magnitude (GGM) filter is similar to the Sobel filter, calculating the magnitude of the image gradient assuming Gaussian derivatives. By varying the Gaussian width, σ, the filter is sensitive to gradients on different scales. GGM filtering has the advantage of being a simple convolution applied to the data and is unlikely to introduce artefacts.

We applied the GGM filter from SCIPY (http://www.scipy.org/) to the exposure-corrected background-subtracted image using $\sigma = 1, 2, 4, 8, 16$ and 32 detector pixels, yielding the images shown in Fig. 2. Regions with large gradients, such as edges, are lighter, while flatter SB areas are darker. Point sources were first removed from the input image to avoid their contamination of larger structures. They were initially identified using WAVDETECT but manually edited to exclude false detections when it became confused by the bright central X-ray structures. The values of pixels in the removed source regions were replaced by random selections of those in the 1-pixel-wide areas immediately surrounding each point source.

The ability of the filter to detect features is a function of the SB in the region of interest and the magnitude of the gradient. In the cluster outskirts where the number of counts per pixel is low, the small length scale filters cannot detect gradients unless they are very large. This is the case with normal X-ray images, where the detectability of structures depends on their size, SB and contrast with their surroundings. The noise in the images, however, is seen as azimuthal structures. As the largest SB gradient in a cluster is radial, Poisson fluctuations in the X-ray image will amplify or weaken this radial signal. Therefore noise in the gradient image lies perpendicular to the gradient in the original image.

To show the gradients on different scales in a single image (Fig. 1 bottom panel), we added the GGM-filtered images with radial scaling factors. These radial scalings were applied to increase the contribution of small scales to the centre (measured from the central radio nucleus) and reduce the contribution of large scales there. We experimented with scaling factors, finding linear summations of the different filtered images do not introduce features which are not present in the individual filtered images. We note that the image does not accurately show the relative magnitude of features but instead highlights those features which are there. The image shows a number of edges and flat structures around the nucleus and inside the western cold front (see Section 2.5). Further discussion of gradient filtering and its application to other X-ray cluster data sets will be made in a forthcoming paper.

2.2 Temperature and metallicity maps

Fig. 3 shows maps of the temperature and metallicity, obtained by spectral fitting (Appendix A2). The cool central plume and cooler regions inside the western and eastern SB edges can be clearly seen. From the core is another plume-like cooler structure extending north-westwards towards the western edge. Outside the edges the temperature is relatively flat, although there may be a cooler region towards the north-east.

The metallicity map contains a great deal of structure. There is a previously reported high-metallicity region inside the western cold front edge, where the ICM is cooler (Sanders & Fabian 2002; Fabian et al. 2005). The abundance distribution, however, is not steadily rising, but is rather flat with fluctuations. There are strong variations in metallicity (see Section 2.6) with a characteristic length scale of around 20 arcsec (∼5 kpc; see Appendix A4). On the eastern side of the cluster, outside the eastern SB edge (Fig. 1), is another region of higher metallicity gas with a tail-like appearance.

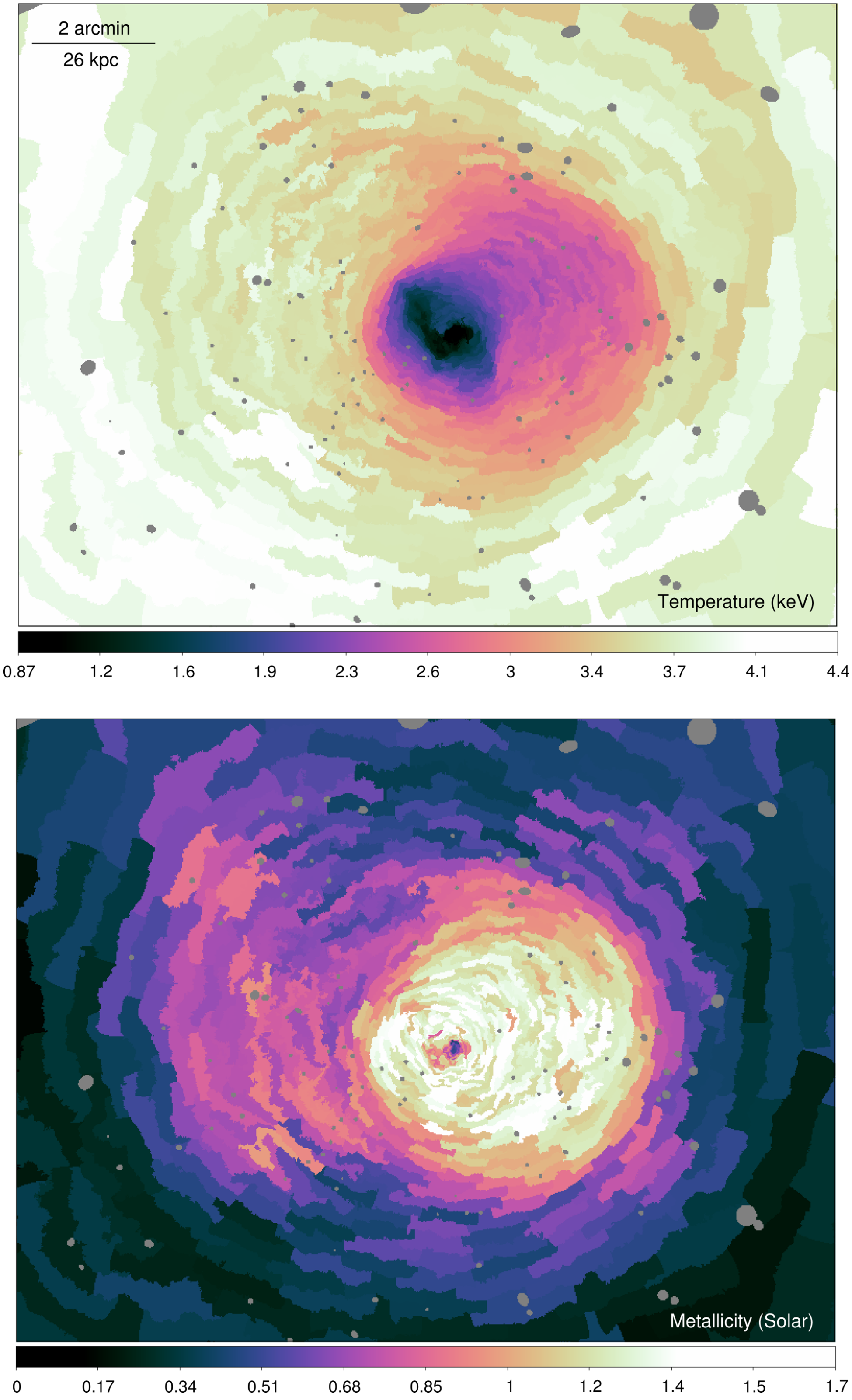

Figure 3. Temperature and metallicity maps of the cluster using regions with S/N = 100. The temperature map shows the single-component temperature. The metallicity map shows the results from single- or two-component fits, depending on which is preferred. Grey regions indicate excluded point sources. Uncertainties in the temperatures vary from 0.6 per cent in the centre to 2 per cent to the east of the western edge and 3.5 per cent at large radius. Metallicity uncertainties are typically from 0.05–0.10 $Z_{\odot}$, excluding the very centre.

2.3 Sloshing

We compare the SB deviations in the cluster to the metallicity and temperature in Fig. 4. There is a low-density, high-temperature material on the opposite side of the core to the high-density, low-temperature material behind the western cold front. This material appears to sweep from the south through the east and towards the north. The plot shows striking correlations between SB, temperature and density deviations. The western cold front is labelled E2. There are also two edges in metallicity and SB in the opposite direction towards the eastern side of the cluster (marked E1 and E3), closer to the Cen 45 subcluster. In addition, there is a further edge outside the western cold front, going from the westernmost point of the cold front and extending towards the north, with more metal-rich gas inside it (E4). Further to the north is the high-metallicity region already noted by Walker et al. (2013). There are hints that there is an SB edge to the north of this feature, with lower metallicity outside it (E5). The SB enhancement towards the north-west of Fig. 4 may be the structure found by Churazov et al. (1999, see their fig. 3), suggested to be stripped gas from NGC 4696B.

In Fig. 5 are shown three rectangular profiles across the cluster in an east–west direction. One passes through the nucleus, while one is north of it and the other south. In some regions there is excellent correlation (between SB and metallicity) or anticorrelation (of SB or metallicity with temperature) between the variables, but this is not always the case. For example, in the central region, the bright, cool, plume is relatively low in metallicity. There is also a fairly strong east–west SB gradient, which makes the fluctuations difficult to see.

Fig. 6 shows radial profiles in metallicity in four quadrants to the north, south, east and west. Despite small-scale variation, the overall metallicity profile inside the western edge (roughly 40 kpc radius) is remarkably flat. In addition there remains a central drop in metallicity, which we discuss further in Section 5. In the eastern sector, there is a much smaller region of flat metallicity towards the cluster core. However, the tail-like structure has a flat metallicity profile which drops outward of 60–70 kpc.

The spatial correlation between SB and metallicity enhancement, and anticorrelation with temperature is a typical signature of sloshing and has been found in simulations as well as other observations (e.g. Virgo, Roediger et al. 2011; A 496, Roediger et al. 2012; Perseus, Simionescu et al. 2012; A 2029, Paterno-Mahler et al. 2013). Similarly, sloshing in the cluster can distort and induce asymmetries in the distribution of metals about the central galaxy.

The gravitational perturbation by the merger of the Cen 45 subcluster may have started these sloshing motions. This is suggested by the alignment of the larger scale SB deviations along the axis of the merger (Fig. 4). After the interaction by the perturbing system, cold fronts move outwards with time (e.g. Ascasibar & Markevitch 2006). The A 496 system, which has a similar temperature to Centaurus, was simulated by Roediger et al. (2012), who found that the radial evolution of the cold front mainly depends on the cluster potential. The radii of the eastern and western inner Centaurus cold fronts (19 and 42 kpc, respectively) are similar to the fronts in their 'distant' run after 1 Gyr (see their fig. 7). The circular symmetry of the features suggest that the sloshing gas motions are close to being perpendicular to the line of sight, as pointed out by Ascasibar & Markevitch (2006). In this case, the perturbing system is not moving in the plane of the sky. It is not possible to tell whether Cen 45 is the perturber based on its position, velocity and the time since the interaction. Indeed, Cen 45 may not be on its first pass through the system and could be gravitationally bound.

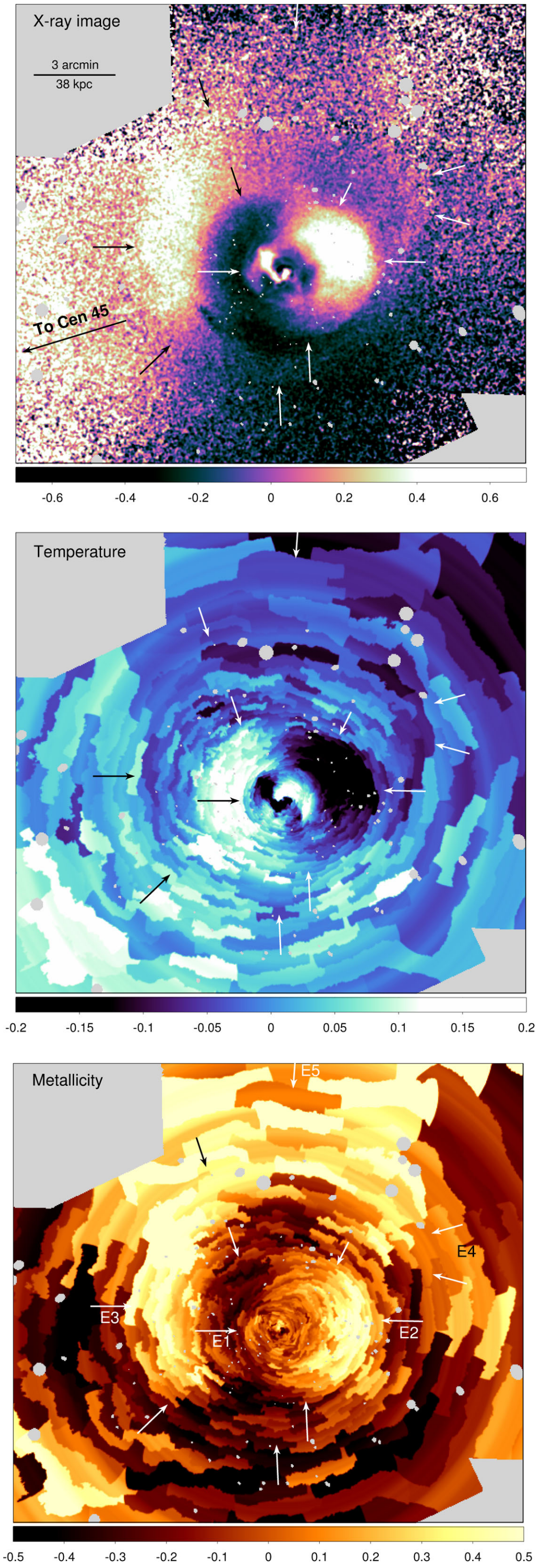

Figure 4. Fractional difference from the average at each radius for X-ray 0.5–7 keV SB, temperature and metallicity. The X-ray image was smoothed by a 2 arcsec Gaussian. The temperature and metallicity maps used the same data as presented in Fig. 3. Arrows mark edges (discussed in text). Also shown is the direction of the merging Cen 45 subcluster.

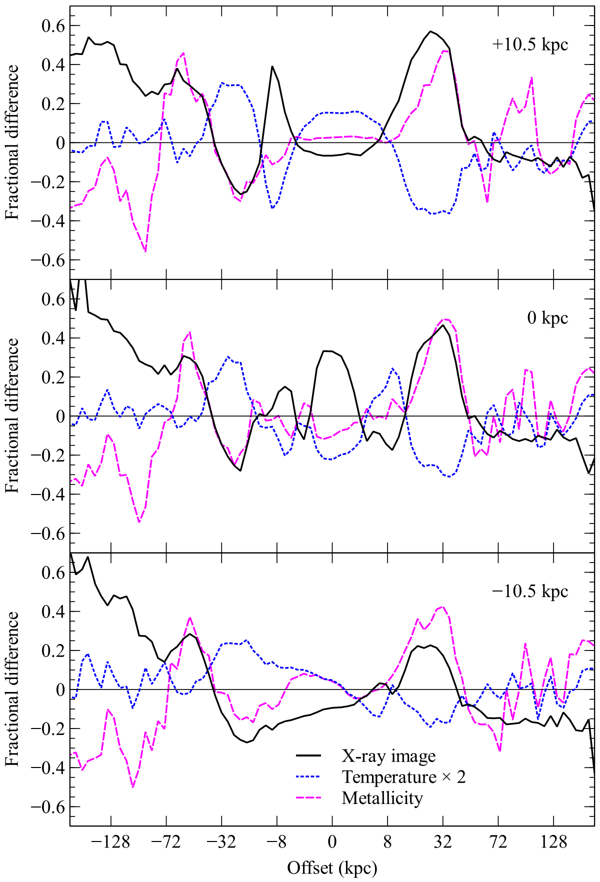

Figure 5. SB, temperature and metallicity fractional residual profiles in an east–west direction (west is positive) across the centre of the cluster with three northerly offsets (−10.5, 0 and 10.5 kpc), computed from Fig. 4. The width of each strip is 8.4 kpc. The horizontal axis has a square-root scaling. Note that the temperature profiles have been scaled by a factor of 2.

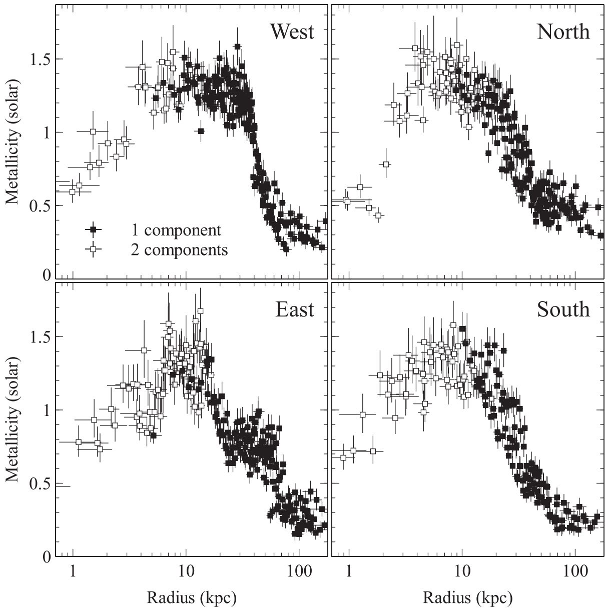

Figure 6. Radial metallicity profile of the map in Fig. 3 split into 90° sectors. The number of components used in the fits is indicated by open or closed symbols. Horizontal error bars show the radial range of each bin.

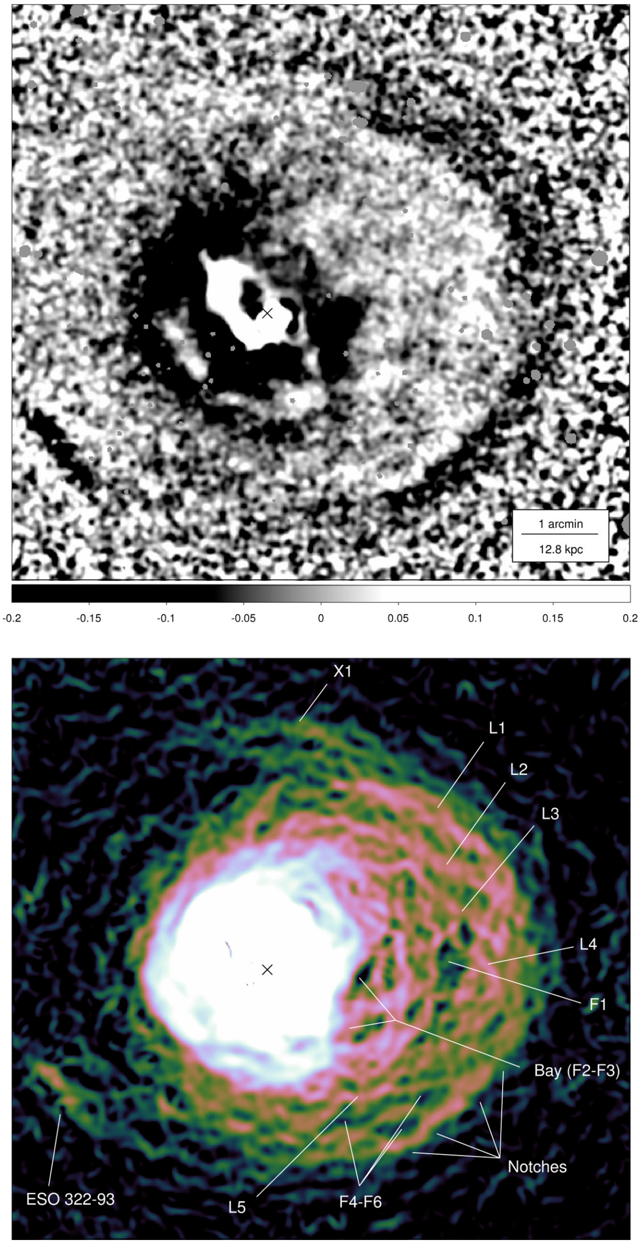

Figure 7. Top panel: unsharp-masked 0.5–7 keV image. This is the fractional difference between Gaussian-smoothed images with $\sigma = 2.0$ and 15.7 arcsec, after masking out point sources. '×' marks the central nucleus (see Section 3). Bottom panel: GGM-filtered image of the same region, using $\sigma = 7.9$ arcsec, taken from Fig. 2. The labelled features are described in Section 2.5.

2.4 Western cold front

The western cold front in Centaurus is one of the clearest and nearest examples known in a cluster, spanning nearly 180°. The pressure across the edge is continuous, confirming it is a cold front (Appendix A3). Fig. 7 (top panel) shows an unsharp-masked image of the centre and cold front region, highlighting the SB fluctuations around the front and within the central region. The edge is not perfectly smooth; the south-western side appears to be where it is sharpest and directly west it appears broader. To the north and south of the cold front there is a rapid transition from a sharp edge to a weak or non-existent edge. However, some circular structure may continue on in the north-east and south-east directions. There appear

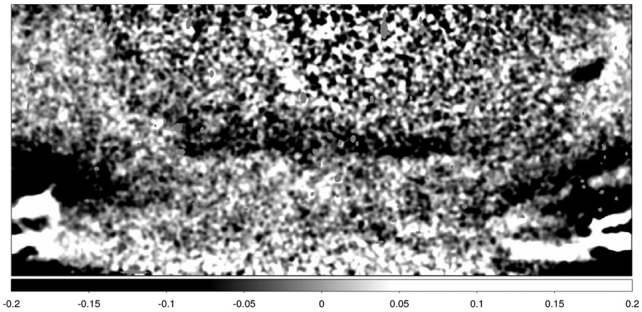

Figure 8. Unsharp-masked image of the cluster remapped to have radius and angle axes, with a centre chosen to make the western cold front lie at constant radius. Horizontally it spans 360° from east (left), through north, then west (centre), then back to east (right). Radius runs vertically from 2 (bottom) to 68 kpc (top). The 0.5–7 keV input image was rebinned into 0.1 kpc by 0°.25 pixels. Unsharp masking was then applied, using the fractional difference between maps smoothed by 4 and 32 pixels.

to be a number of 'notches' into the edge on length scales of ∼7 kpc. The notches along the edge can also be seen in a gradient filtered X-ray image (Fig. 7 bottom panel). We discuss the SB features inside the front in Section 2.5.

The deviations from a circular cold front can be clearly seen if the image of the cluster is remapped to radial and azimuthal coordinates (Fig. 8). The notches appear as wave-like irregularities on the straight edge. The edge is best represented by a circle with a centre at RA 192.18325 and Dec −41.31048 (marked by the sectors in Fig. 7), 11 kpc to the west of the nucleus.

To quantify the variation and width of the edge around the front, we fit models to SB profiles extracted in 27 independent 10° sectors spanning 270°, covering the 180° towards the west where the front is visible and 45° beyond this in either direction. This analysis is similar to that presented in Werner et al. (2016). We fit a broken power law with a broadened edge model to the profiles (see Appendix A3). Fig. 9 shows for each sector the radius of the front, the jump magnitude, the width and the power-law indices to either side of the edge.

Between the north and south, where the edge is well defined, the jump radius is fairly constant at 31 kpc, with sector-to-sector variations of about 1 kpc, likely due to the notches around the edge. Immediately west, the front is at its broadest at 4 kpc, but it is much narrower to the north-west and south-west. In some locations the edge appears narrower than 1 kpc. Where the front is narrowest towards the south-west, for example in the sectors between 60 and 80°, the 1σ upper limits on the edge width are ∼0.3 kpc (accounting for the point spread function (PSF) at the edge in these sectors). If there are no magnetic fields, in the north-west direction the density and temperature imply values for the collisional electron mean free path of 0.18 and 0.36 kpc (0.8 and 1.7 arcsec), interior and exterior to the front, respectively. In the south-west these increase to 0.30 and 0.48 kpc (1.4 and 2.3 arcsec), respectively. Where the front is narrowest to the south-east, our upper limits are similar to the electron mean free path.

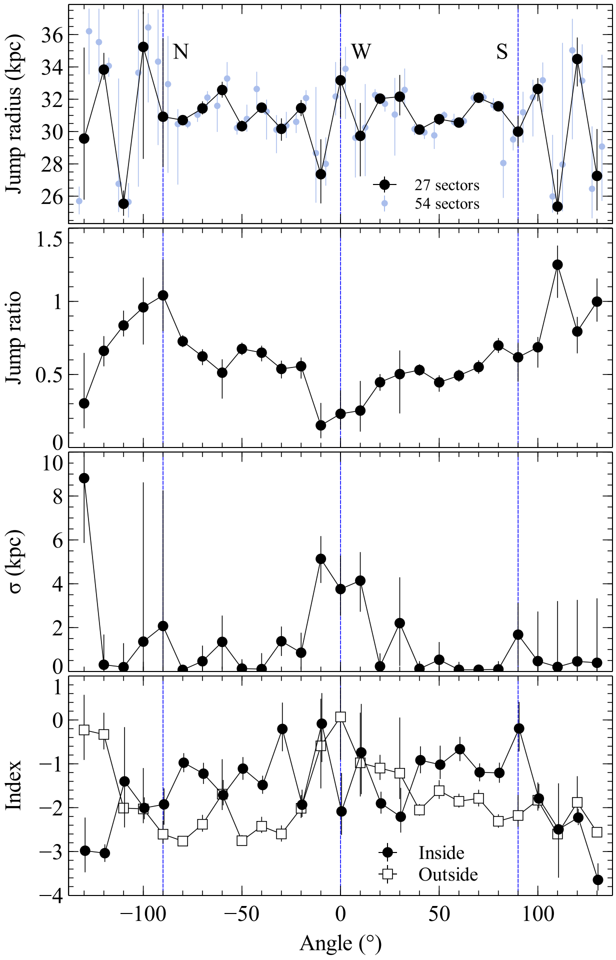

Figure 9. Fit parameters for the profiles of the 27 sectors around the western cold front from the north-east (−130°) to south-east (130°). These are the median and 1σ percentiles obtained from the analysis (Appendix A3). Shown are the radius of the jump, the ratio in emissivity outside to inside (the jump ratio), its width (σ) and the power-law indices of the emissivity inside and outside. For the radius we also show the results using twice the number of sectors.

The emissivity of the ICM decreases outwards over most of the front to around 60 per cent of the interior value, implying that the density decreases by around 20 per cent, which is in agreement with spectral measurements (Appendix A3). However, immediately to the west the fits prefer an 80 per cent SB decrease. In the same region the power-law index of the model outside the jump is flatter and the edge is wider. It is clear from the unsharp-masked and filtered images in Fig. 7 that the edge is much less distinct immediately to the west at the most extreme part of the front. There may also be an SB edge which extends from the westernmost point of the front to the north-west. This can be seen where SB edge E4 apparently connects to the cold front E2 (Fig. 4). This feature can also be seen as the enhancement in the remapped cluster image (Fig. 8) from the centre of the front extending upwards (to larger radius) and leftwards (north-west).

Outside the 180° sector where the edge is obvious, the SB fits imply that there is some sort of jump or break in SB in the radial range examined. The allowed jump radii vary considerably, however, and are unlikely to correspond to the same physical features in the profiles.

The notches along the edge of the western cold front (Figs 7 and 8) are consistent with Kelvin–Helmholtz instabilities (KHIs) of length scales of ∼7 kpc along the edge. KHIs in clusters were first seen in simulations (Roediger et al. 2011; ZuHone, Markevitch & Lee 2011). A kink, which may be a large KHI, has been observed in Abell 496 (Roediger et al. 2012). Similar notches of length of a few kpc have also been seen in the cold front in the Virgo cluster (Werner et al. 2016). These notches likely make the radius of the cold front appear to vary by ∼1 kpc (Fig. 9) between the north and south. Comparison with simulations of cold fronts including varying levels of viscosity or magnetic fields suggests levels of viscosity of around 10 per cent of the *Spitzer* value are consistent with the data (Roediger et al. 2013; ZuHone et al. 2015). Larger amounts of viscosity smooth out all instabilities, while instabilities grow very large with no viscosity or magnetic fields.

2.5 Linear structures inside the front

Using shorter observations, we previously detected ripple-like SB fluctuations using Fourier high pass filtering (Sanders & Fabian 2008). These quasi-periodic fluctuations were also seen in SB profiles in three sectors (along the north-east, south-west and north-west directions). We interpreted these features as sound waves generated by AGN activity.

Examining the unsharp-masked image (Fig. 7 top panel) there are a number of SB fluctuations with a similar ∼5–10 kpc length scale to the previously found fluctuations. They are also similar in size to the notches along the cold front (Section 2.4). However, they do not appear to have a periodic structure. Creating SB profiles using the same sectors as in Sanders & Fabian (2008), obtains consistent SB profiles and residuals to β model fits, showing that the fluctuations are robust.

Using a GGM filter on the data instead of unsharp-masking (Fig. 7 bottom panel) finds a number of quasi-linear features (labelled L1–L5). These straight edges have corresponding features in the unsharp-masked image, but the GGM filter appears to be a much more powerful tool for detecting and connecting these edges in SB. All of the labelled structures in Fig. 7 (bottom panel) can be seen as SB edges in the raw data when examined closely. The structures are also apparent in the multiple-scale GGM-filtered image (Fig. 1 bottom panel).

We tested that these features are significant by similarly filtering a Poisson realization of a heavily smoothed cluster image, finding that the noise was at lower levels. In addition, all the labelled features can be seen by closely inspecting the raw images. L1–L4 are approximately parallel to each other. L1 and L4 (and perhaps L2 and L3) also appear to bend with a sharp angle close to the edge of the cold front. The image also highlights some flat SB regions (F1–F6). The bay (discussed in Section 3) appears as two flat regions surrounded by steep gradients. There are also flat regions closer to the edge of the front (F1 and F4–F6). To the north is an extension of the cluster emission extends northwards (X1).

Several of the identified linear features L1–L6 appear to have an approximately regular separation of ∼5 kpc. L1–L3 seem to have a sharp bend near the cold front, suggestive of waves reflecting off a boundary. The temperature on the outside of the cold front is a factor of ∼1.4 greater than inside. Therefore the critical angle for total internal reflection at the cold front is 58°. If the features are sound waves, then they lie above this critical angle, and so it is possible that the bends at the cold-front edge are caused by total internal reflection of sound waves. Alternatively, variations in sound speed could cause the fronts to bend if the wave passes through a sharp temperature gradient at an angle.

The 5 kpc spacing corresponds to a 6 Myr time-scale at the sound speed at 2.5 keV temperature. This time-scale is similar to the age of the inner shock and cavities. It is therefore plausible that the structures could be generated by AGN activity. The quasi-periodic nature of the features argues against the features being turbulence generated by the AGN. We analyse these fluctuations quantitatively in Walker, Sanders & Fabian (2015) and examine whether they could contribute significantly to AGN feedback heating.

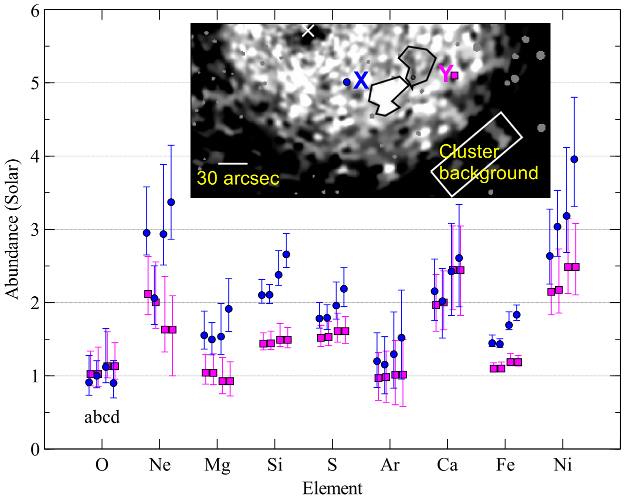

Figure 10. Comparison of the metallicity in adjacent high (X) and low (Y) metallicity regions, fitting (a) 1 and (b) 2 component(s), blank-sky background, and (c) 1 and (d) 2 component(s), cluster background (see Appendix A4). The inset metallicity map was created from S/N = 40 regions.

Alternatively, the structures may be unrelated to the AGN but instead caused by sloshing. The sloshing simulations of Roediger et al. (2013), in particular their fig. 8, shows features similar in appearance. KHIs on the curved 3D surface of the cold front can be seen as projected features inside the cold front edge. The interaction of KHIs at the cold front, combined with the slow outwards motion of the cold front can also give rise to turbulence inside or underneath the cold front, which also adds fine structure. Linear features were also found by Werner et al. (2016) inside the M 87 cold front. They suggested that these could instead be generated by the amplification of magnetic field layers by sloshing, as found in the simulations of ZuHone et al. (2011, 2015).

2.6 Metallicity blobs

There are fluctuations in metallicity interior to the western cold front on ∼5–10 kpc scales (Fig. 3). These features are robust against changes to the binning scheme. We compared two neighbouring regions offset from the nucleus with high (X) and low (Y) metallicity (Fig. 10) to confirm that these structures are significant. Fitting the spectra separately, we obtained the metallicities using one and two temperature component fits, and for two different background spectra.

The Si and Fe abundances are greater in region X for every model. The Fe metallicity is 30 per cent greater in region X using a blank-sky background, increasing to 55 per cent if a cluster background is used. It should be noted that if a blank-sky background is used, the Fe metallicity calculated from the Fe-K lines is consistent (∼1 $Z_\odot$) between X and Y. However, a cluster background makes the Fe-K line strength consistent with the increase in metallicity seen in the Fe-L lines. The cluster background is likely more realistic, as we know that there is projected cluster emission. Within the uncertainties, the enhancements in the other elements are consistent with the Fe increase. There is no preference for increased amounts of Type Ia or Type II supernova products in the high-metallicity region.

We estimated the effects of projection by considering an 8^3 kpc^3 enhancement in metallicity at 25 kpc radius, using the profiles across the SW front (Appendix A3). For regions of this size, the measured enhancement is likely suppressed by a factor of ∼4. Therefore this blob has ∼5 times the metallicity of the nearby low-metallicity material, assuming that the simple model of an enhanced cubic blob is correct. Region X would contain an enhancement of around $10^6\,\mathrm{M}_\odot$ of Fe over region Y.

The flatness of the western metallicity profile and sharpness of the cold front edge implies high effective central diffusion rates which rapidly drop with radius (Graham et al. 2006; Walker, Fabian & Kosec 2014). The existence of the compact high-metallicity regions argues that diffusion by stochastic gas motions is low. In contrast, sloshing of gas in the potential well does not lead to broadening of the distribution (Roediger et al. 2012), but results in asymmetric and distorted distributions. If the AGN bubbles drag dusty clouds of high-metallicity gas produced by stellar mass-loss from the core of NGC 4696 to larger radius, this will naturally flatten out the central peak and give the observed effective diffusion coefficient which rapidly declines with radius (Panagoulia, Fabian & Sanders 2013). In addition, this intriguingly raises the possibility that the high-metallicity regions are metal-rich materials uplifted from the galactic centre by AGN bubbles. High-metallicity blobs on similar scales have appeared in other clusters which have good quality data (e.g. Perseus, Sanders & Fabian 2007 and Abell 2204, Sanders, Fabian & Taylor 2009a) and could be produced by a similar process.

If the material was injected into a much smaller region and has expanded to size L over a time-scale t, the diffusion coefficient is $D \sim L^2/(24t)$ in three dimensions. Using the sloshing time-scale (1 Gyr; Section 2.3) and a size of 8 kpc, this translates into a diffusion coefficient $D \sim 10^{27}\,\mathrm{cm}^2\,\mathrm{s}^{-1}$. If the cavity age (e.g. 10 Myr; Section 3) is a more appropriate time-scale because the blobs are uplifted by the AGN, then the diffusion coefficient would be two orders of magnitude greater.

3 NUCLEAR REGION

3.1 Images and spectral maps

Fig. 11 (top panel) shows an RGB image of the central ∼30 kpc of the cluster around the central radio source. Cool structures in the cluster appear as red in this scheme. In Fig. 11 (bottom panel) is a labelled image of the same region, with partial unsharp-masking. Obvious is the soft cool plume-like structure extending to the north-east (Sanders & Fabian 2002). In these new, deeper, observations it can be seen that the plume is made up of at least three separate filaments. There are the two strong central cavities in the X-ray either side of the nucleus which are filled with high-frequency (GHz) radio emitting plasma (Taylor et al. 2002). Connecting the plume to the nucleus is an SB edge, labelled the inner edge. Between this edge and the plume appears to be a SB depression. The plume appears to extend through the edge, ending a few kpc beyond that. The inner edge may represent the edge of an egg-shaped region of enhanced SB. To the south-east of the core is another cool filament with a hook-like shape. There is an SB edge to the south-west, with an unusual negative curvature. We name it the bay, as it looks similar to the bay seen in the core of the Perseus cluster (Fabian et al. 2006). Similar structures are also seen in Abell 1795 and Abell 2390 (Walker et al. 2014).

The large number of counts available in this data set allow us to make detailed X-ray images of the very central regions in different energy bands (Fig. 12). The 0.5–1 keV band is sensitive to cool (∼1 keV) gas, while the 1.5–7 keV band is sensitive to hotter material. The radio nucleus, as noted by Taylor et al. (2006), is offset to the north-east of a ridge of bright, soft X-ray emission. The nucleus also does not lie in the geometric centre of the two inner cavities. Also shown in Fig. 12 is a projected X-ray temperature map of the same region (taken from Fig. 13). The lowest temperature material is strongly correlated with the soft emission, although there is not a complete correspondence.

Maps of the central temperature, XSPEC normalization per unit area and pseudo-pressure are shown in Fig. 13. The normalization per unit area scales with the density squared and the line-of-sight depth. The pseudo-pressure is the temperature multiplied by the normalization per unit area, scaling as the projected thermal pressure times the line-of-sight depth. On the left-hand side are the projected quantities. On the right are shown the fractional deviations from spherical symmetry.

The temperature map shows that the soft-X-ray-emitting structures, including the plume, seen in the X-ray images, are indeed cooler gas. The overall temperature decreases towards the core of the cluster. The temperature deviation map shows deviations in projected temperature are around 30 per cent. The map shows an extension of cool material in roughly the opposite direction to the plume from the nucleus. The normalization map shows the dense plume structure and the dense shells around the two inner cavities. Examining the non-spherical structure, there are a number of depressions visible in the residuals, which we assign the letters A–H. The pressure maps show the thermal pressure is lower inside the two central cavities and also towards the end of the plume and towards the south-west, in roughly the opposite direction.

3.2 Shock around nucleus

There is a shell-like enhancement which surrounds the central nucleus (Fig. 14), not clear in the previous images. This shell appears to split into two separate fine edges to the south-east, separated by 3 arcsec (0.6 kpc). The north part of the shell can be seen in the RGB image (Fig. 11) as a blue rim to the north of the red central emission. The shell has a radius of 9 arcsec (1.9 kpc). The nucleus is offset 3 arcsec (0.6 kpc) to the south-east from the geometric centre of the shell, in the direction of the splitting of the edge.

Its morphology suggests that it may be a shock generated by an outburst of the central nucleus. This is consistent with the X-ray emission from the feature being hard. However, we do not see an obvious SB enhancement within the shock, but just its edge, which may be due to the complex density and temperature structure at the core of the cluster. The shock appears to be overlapping the central cavities. If the cavities and shock were spatially coincident, it is unclear into what the shock is shocking. A possible explanation is that the cavities are offset along the line of sight from each other and the shock lies between the two and around the nucleus.

We do not know the speed of the shock, but given the sound speed for material at 1.1 keV, an upper limit for its age would be ∼3.5 Myr. The outer parts of central bubbles beyond the shock are at a maximum projected radius of around 5.5 kpc, which would imply that they are only a few times older than the shock, unless projected radii are much larger than intrinsic distances, which their morphology suggests is not the case. Estimates for the ages of the inner bubbles in Centaurus range from 6 to 22 Myr (Rafferty et al. 2006). This implies that there are repeated outbursts from the nucleus in Centaurus on time-scales of 3–19 Myr.

A shock would explain why the X-ray-coolest gas is not the closest to the nucleus, although this could alternatively be explained by sloshing. If there was a non-symmetric temperature distribution around the nucleus before the shock was launched, the varying sound speed might explain why the nucleus is not at the shell centre.

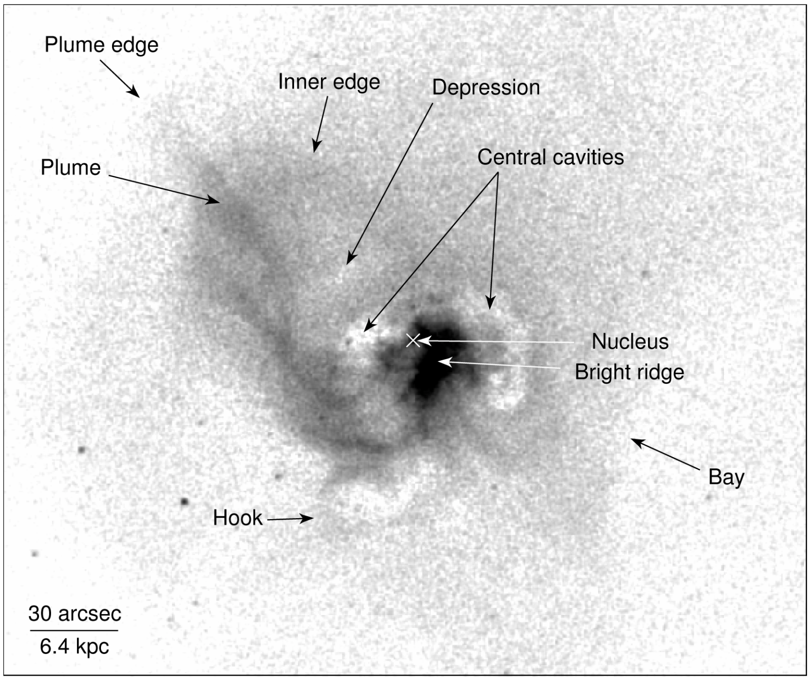

Figure 11. Top panel: RGB image of the cluster centre. The bands 0.5–1, 1–1.5 and 1.5–7 keV are shown as red, green and blue, respectively. Images were extracted using bins of 0.5 detector pixels (0.246 arcsec) and smoothed by a Gaussian of width 0.492 arcsec. The image measures 2.8 by 2.3 arcmin (35 by 29 kpc). Bottom panel: partially unsharp-masked 0.5–7 keV grey-scale image showing labelled features, constructed by taking the X-ray data in 0.246 arcsec pixels and smoothing by a Gaussian of width 1 pixel and subtracting the 0.5 times the image smoothed by 64 pixels.

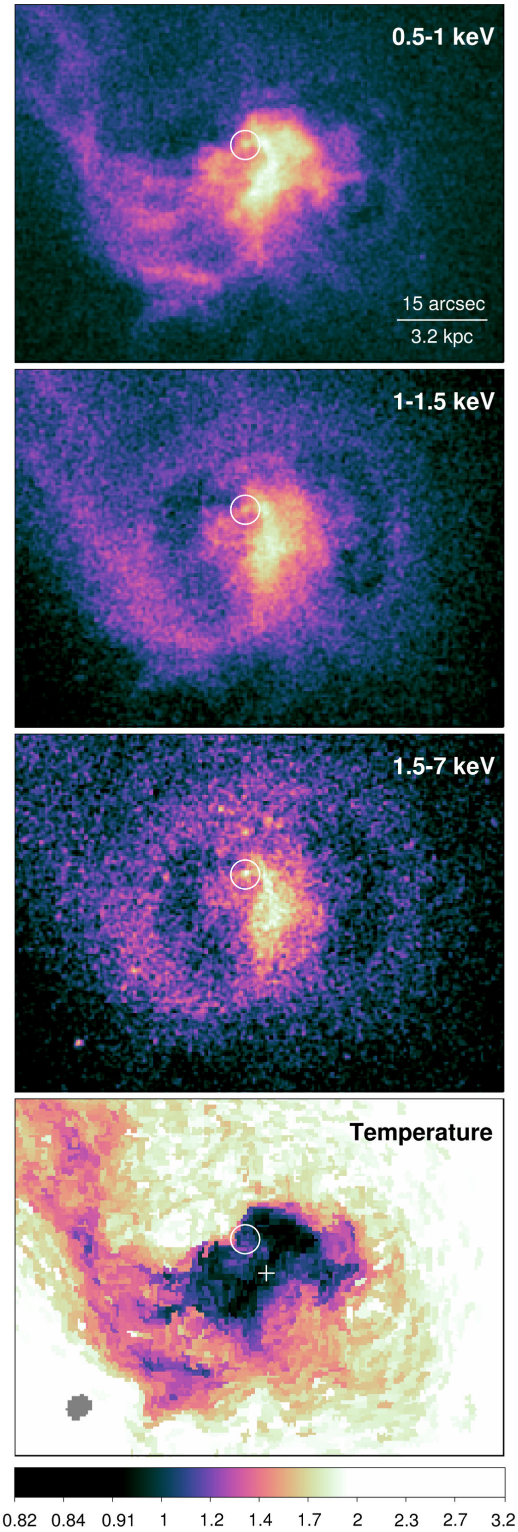

Figure 12. Detail of the central regions in three energy bands and comparison temperature map. X-ray images were created with 0.246 arcsec binning with 1 pixel Gaussian smoothing. A 2.4 arcsec radius circle marks the radio nucleus and '+' shows the X-ray centroid.

Indeed, the colder material seen to the west might have reduced the shock radius in this direction. This colder material, however, may only lie close to the nucleus in projection and could be outside the shock region. The very central high-frequency radio emission appears to be bounded by the shell edges to the north and south (Section 3.3).

3.3 Interaction of radio source and ICM

The central radio source PKS 1246−410 was observed in 2013 and 2014 using the Karl G. Jansky Very Large Array (VLA) in the A and B configurations between 8 and 10 GHz, with a total of 8.2 h of time on source. Analysis details and first results are presented in Grimes (2014). The intensity map is shown in Fig. 15(a). There are a number of edges in the radio image, which we highlight by applying a GGM filter (b). The filtered image suggests that the inner part of the source is extended along the north–south direction, changing to the east–west on larger scales. The bright nucleus is also extended in the north–south direction, in agreement with the jet on smaller scales in VLBI observations (Taylor et al. 2006).

We compare the radio emission at 9 and 5 GHz with the soft X-rays (c), examining the central region using a GGM-filtered soft X-ray image (d). It can be seen that the edges in the soft X-ray emission (as traced by the GGM-filtered image) extend along the direction of the radio source or around its edges. This is consistent with the skin effects surrounding the radio source identified in the RM analysis of Rudnick & Blundell (2003). Examining the harder X-ray emission (e) we see that the rims of the X-ray cavity match the extent of the radio source. In addition, edges in the inner part of the radio source closely follow the edge of the shell-like structure, as seen in a GGM-filtered harder image (f). The edges in the radio source can clearly be seen in the GGM-filtered image (b).

At lower frequencies, the radio emission is connected to features in the X-ray image and pressure map (Fig. 16; Taylor et al. 2002). At 1.6 GHz, in addition to emission in the central cavities, there are extensions to the north and south. In the south, the emission appears to bifurcate into extensions R3 and R4. Region R4 is coincident with an area of lower pseudo-pressure and a depression in the X-ray image (labelled E in Fig. 13). To the north there is an extension in the radio source, R2, along the direction of the plume in a region lower in pseudo-pressure. At 330 MHz frequencies, measured using the VLA, R2 extends into the lower pressure region R1 and R4 continues south along a lower pressure channel to R5. There also exists a spur of emission into a lower pressure region R6.

The radio emission switches from a north–south direction on jet scales, to east–west in the inner cavities to north–south again on larger scales. The radio source and X-ray emission are connected from sub-kpc scales to several tens of kpc. In the very inner region, the high-frequency radio emission shows edges coincident with the inner shell, or shock. In the inner 2 kpc, there are edges in the soft X-ray emission which clearly trace along the direction of the radio source, including an edge running along its mid-point and a sharp edge immediately to the south of the inner radio source, south of which is a bright ridge of X-ray emission.

3.4 Cavities

There are a number of SB depressions in the core of the cluster, most easily seen labelled in the residual normalization map (Fig. 13) and the GGM-filtered image (Fig. 1). A and B are the central cavities coincident with radio emission. C is the depression between the nucleus and plume, marked by the 'inner edge' in Fig. 11. D is the depression bounded by the 'bay' structure. E is also associated with a depression in the thermal pressure, and lies near the 'hook' structure (which itself seems to surround another cavity, I). F, G and H are further depressions. All of these features could be generated

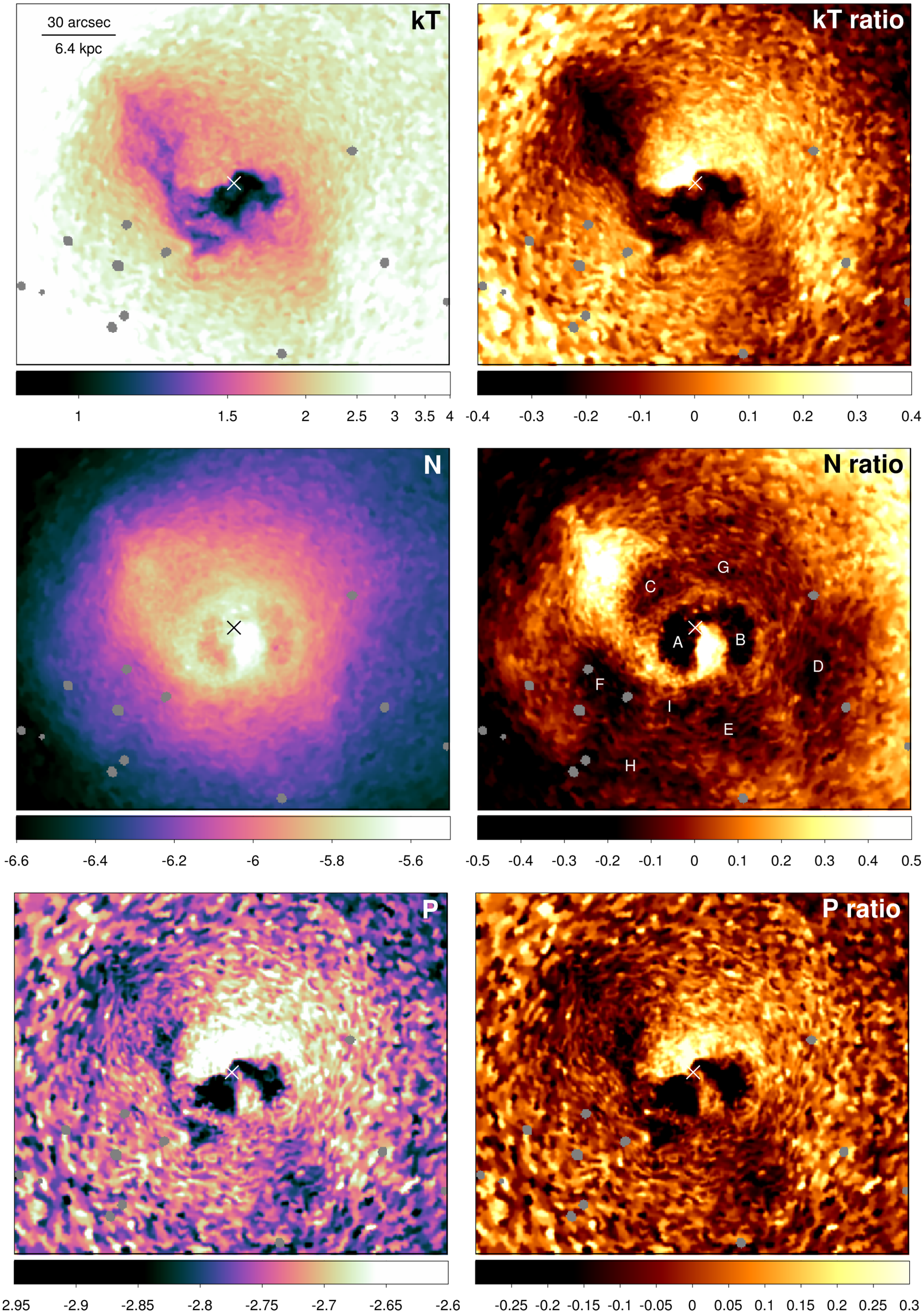

Figure 13. Central spectral maps (left) and fractional deviations from spherical symmetry (right). Analysis details are given in Appendix A5. On the left-hand side are the (top-left panel) temperature in keV, (centre-left panel) normalization (in $\log_{10}$ cm^{-5} arcsec^{-2}) and (bottom-left panel) pseudo-pressure (in $\log_{10}$ keV cm$^{-5/2}$ arcsec^{-1}). On the right-hand side are the fractional deviations from the average at each radius of the respective left map. Maps have been smoothed by a Gaussian of 0.492 arcsec, excluded point sources are shown as circles or ellipses and the central radio source is marked by crosses.

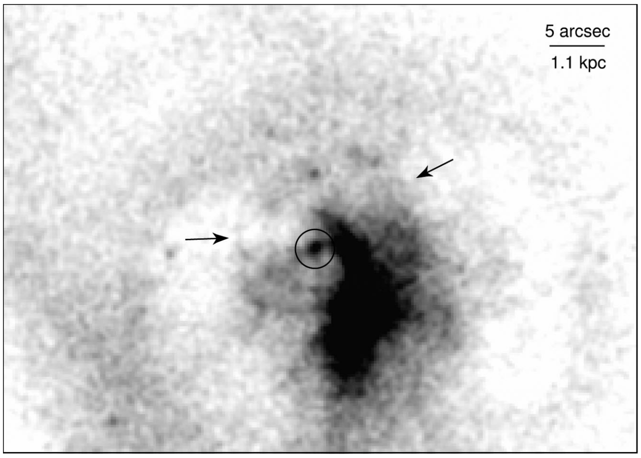

Figure 14. A 1.9-kpc-radius shell-like structure (marked by arrows) seen around the nucleus. The 1–7 keV image was binned in 0.246 arcsec pixels, smoothing by a 1 pixel Gaussian. The radio nucleus position is marked by a circle of radius 1.8 arcsec.

by AGN outbursts, with a large fraction showing some evidence for radio emission (Figs 15 and 16). These include the central cavities (A and B), the cavity towards the plume direction (C), the cavity in the opposite direction (E) and its neighbouring cavity (H). There is also 330 MHz emission at the location of the bay cavity (D). The gradient filtered image on larger scales (Fig. 7 lower panel) shows an SB edge across the bay (it is split into F2 and F3) and there may be further flat SB areas in which could be yet-older cavities (F1 and F4–F6).

A large fraction of the volume in the inner 20 kpc radius, or even further, may be filled by cavities and their ageing electron populations. There are other clusters, such as M 87 (Forman et al. 2007) and 2A 0335+0986 (Sanders, Fabian & Taylor 2009b) which show large number of possible cavities in their core. In Centaurus, the pressure map, however, does not show reductions in thermal pressure at the location of all these cavities, though there are decrements in thermal pressure for A, B, C, E and I. It is possible that displaced thermal gas may mask pressure changes. It is also the case that in other clusters not all extended radio emission is associated with cavities. For example, in Perseus the minihalo emission is correlated with the X-ray substructure (Fabian et al. 2011).

3.5 Shock surrounding inner cavities

There are pressure and temperature enhancements outside the inner cavities towards the north and west (Fig. 13). These could be due to shock heating of the region due to the formation of the cavities. To examine this in more detail, we made deprojected temperature, density and pressure profiles (Fig. 17) across the western inner cavity (the eastern cavity is too close to the plume), and in two comparison regions to the north and south. We note that there are potential problems with deprojecting spectra in a region with a complex structure, although the results are qualitatively consistent with the projected maps. The cavity is clearly seen in the density profile (the 7th radial bin), where only an upper limit can be obtained.

Immediately outside the cavity the temperature is relatively low (1.2 keV), but jumps up by 40 per cent in the next bin to 1.7 keV. It then stays flat over ∼3 kpc, then rises from 8 to 13 kpc, then flattens again. In comparison, the northern profile appears to have the same 1.7 keV temperature plateau from 4.2 to 12 kpc radius, but is even hotter (∼2 keV) inside that at the radius of the cavity. To the south there is a much more gradual rise in temperature with radius. These trends can be seen in the deviation maps of the central region (Fig. 13). Outside the cavity is a 1.7-kpc-thick high-density rim. The profile and images show a similar thicker region in the northern sector. Beyond the cavity rim in the western sector, the density drops by 15 per cent at 9 kpc radius where the sector overlaps with the bay region. The southern density profile does not show the obvious jumps in density beyond 2.6 kpc radius. As there are jumps in both temperature and density, there are corresponding increases in pressure, with the largest pressure increase to the north.

The magnitude of the jumps in temperature, density and pressure are uncertain because we do not know the underlying profiles. We show fits to two sets of points (6–9 kpc and 7.5–9 kpc) in Fig. 17 to indicate the allowed range. The data are not fit beyond 9 kpc because of the density jump, likely associated with the bay region. To the west, comparing the peak value with the fit, the range in temperature jump is 13–24 per cent (although there is a 40 per cent jump in temperature from the bin immediately outside the cavity to the next bin), the density jumps by 18–27 per cent and the pressure by 32–45 per cent. In the northern sector the jumps appear larger. The northern pressure jump is likely between 60 and 130 per cent, while the temperature increases by 40–100 per cent and the density jump is uncertain.

The most likely explanation for these high density, temperature and pressure rims is that they are caused by a weak shock generated by the mechanical action of an outburst of the central AGN on the ICM. Such shocks are seen in other clusters and groups (e.g. Perseus, Fabian et al. 2003; M87, Forman et al. 2007; NGC 5813, Randall et al. 2015). Assuming a $\gamma = 5/3$ gas and using the Rankine–Hugoniot jump conditions (Landau & Lifshitz 1959), the range of density and temperature jump values to the west would imply a Mach number for the shock between 1.1 and 1.2, while the temperature jump ratio implies a value between 1.2 and 1.4. The northern jump in temperature, however, implies a much stronger shock between 1.6 and 2.2. The values are rather uncertain, however, due to the unknown unshocked profiles. The discrepancies between the north and west may be due to the rising cavity entraining cool material which is being mixed into the surrounding ICM to the west, reducing the temperature increase. It is unclear how this could affect the density in this direction, however.

We can estimate the energy that the shock has dissipated in the ICM (as in the Perseus cluster, Graham, Fabian & Sanders 2008). Taking the hard X-ray band image, the western cavity is an ellipse with axes with radii 1.8 and 2.4 kpc and the hard rim has radii 3.3 and 4.2 kpc. Assuming an electron pressure enhancement in the shock of $0.02\,\mathrm{keV\,cm^{-3}}$ and that the shock lies completely around the western cavity, the energy dissipated by the shock is 4×10^{56} erg (using equation 19 in Graham et al. 2008). This compares to the adiabatic energy to expand the cavity $PV = 2 \times 10^{56}$ erg, if the electron pressure for the cavity of $0.07\,\mathrm{keV\,cm^{-3}}$. Therefore the shock energy is around half the energy available ($4\,PV$). The heating power of the shock, using the shock width divided by its speed as a time-scale, is $6 \times 10^{42}\,\mathrm{erg\,s^{-1}}$. This is around 75 per cent greater than the heating power inferred per cavity (Rafferty et al. 2006).

3.6 Dust and X-ray association

In Fig. 18, we compare the optical morphology of the dust lanes in NGC 4696 with the soft X-ray filaments. To remove the smooth stellar component, we constructed an elliptical model. Given a centre, ellipticity and rotation angle, the average at each elliptical radius was computed. This profile was then converted to a 2D image. The

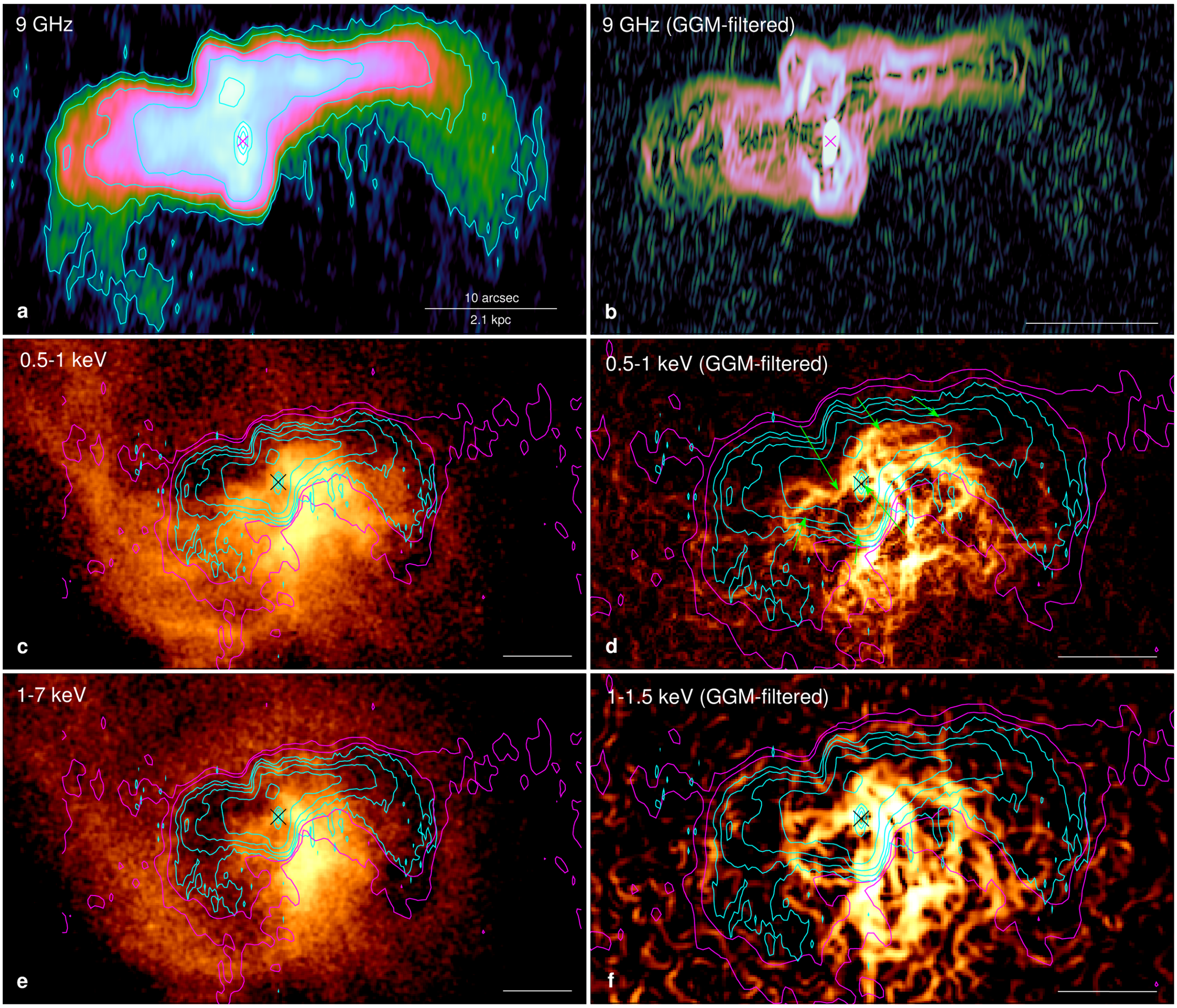

Figure 15. High-frequency radio and X-ray comparison. (a) 9 GHz image with eight logarithmic cyan contours at levels from 4×10^{-5} to 0.0607 Jy beam^{-1}, with resolution 1.15×0.31 arcsec. (b) 9 GHz image applying GGM filter ($\sigma = 0.08$ arcsec). (c) 0.5 to 1 keV X-ray image. Also show are two 5 GHz contours from Taylor et al. (2002) at 0.1 and 0.4 mJy beam^{-1} (magenta). (d) GGM-filtered 0.5–1 keV image, summing the GGM-filtered images with $\sigma = 0.246$ and 0.492 arcsec. Arrows mark regions of high RM. (e) 1 to 7 keV X-ray image. (f) GGM-filtered 1–1.5 keV image ($\sigma = 0.492$ arcsec).

model image was fitted to the data, adjusting the model parameters. Regions containing obvious dust features and bright sources were masked from the data and model during fitting. The ratios of this model to the data are shown in the top panel.

Although the morphology of the dust follows the soft X-ray emission, there is an offset between the regions with the brightest X-ray emission and the dust. We checked point source positions to verify that the astrometry was corrected. The morphological agreement indicates the dust and soft X-rays have a common origin. Either there is a real offset between the components, or there is additional bright X-ray emitting material obscured by dust and associated material. If the dust material is blocking significant X-ray emission it must lie in front of the X-ray emitting material or is well mixed with it. We examined the X-ray spectra of a region between the two rightmost arrows, along the dust lane and a comparison region to the east along the bright X-ray rim. Fitting two-temperature-component models to the spectra did not show any evidence for increased column density in the dust region, either when fixing the temperatures to be the same in the two regions or not. Most of the difference in flux between the regions appears to be around 0.9 keV energy, which argues against absorption which would primarily affect low energies. This would suggest that the soft X-rays and dust are offset, although partial covering models may account for the lack of obvious soft X-ray absorption.

3.7 Plume origin

The reversing SB and temperature structure in the cluster (Fig. 4) suggests that the plume is part of the sloshing morphology of the cluster. Arguing against this origin is that the plume appears to be made up of filamentary multiphase gas, connected to the cluster core (Fig. 11). The southern part of the plume is associated with cold material in other wavebands (e.g. Fig. 18 and Crawford et al. 2005). The spatial coincidence of the radio structure with the plume (Fig. 16) implies that the feature is due to a ghost radio cavity

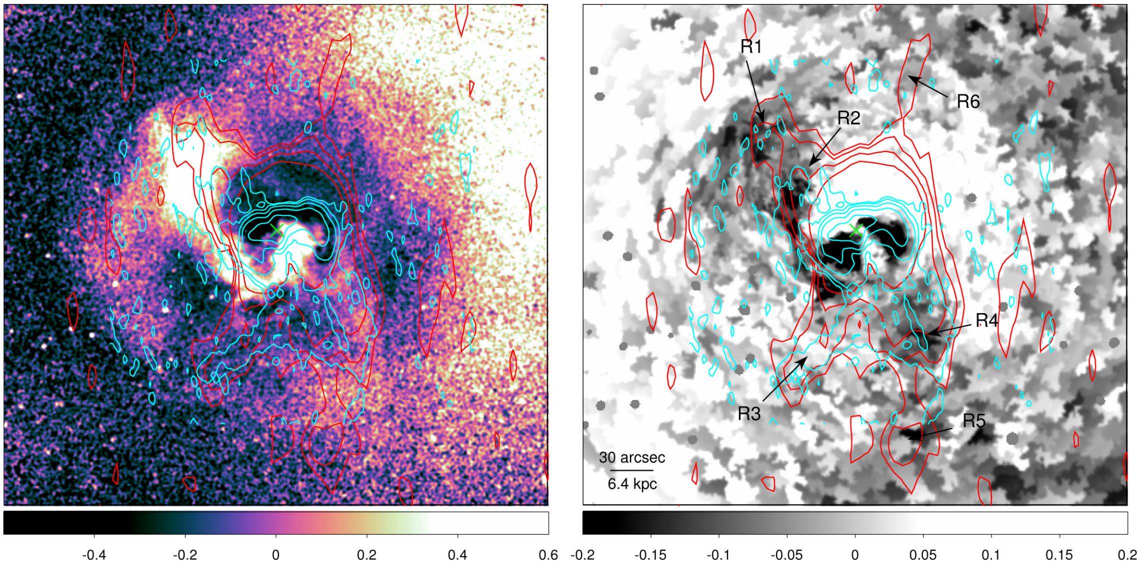

Figure 16. Lower frequency radio and X-ray/pressure comparison. Left-hand panel: 0.5–7 keV X-ray fractional residuals from radial average, showing 1.565 GHz (inner cyan) and 330 MHz (outer red) contours. Right-hand panel: pressure azimuthal fractional residuals using S/N = 40 binning. There are six logarithmic 1.565 GHz contours between 0.2 and 360 mJy beam^{-1} and four logarithmic 330 MHz contours between 10 and 100 mJy beam^{-1}.

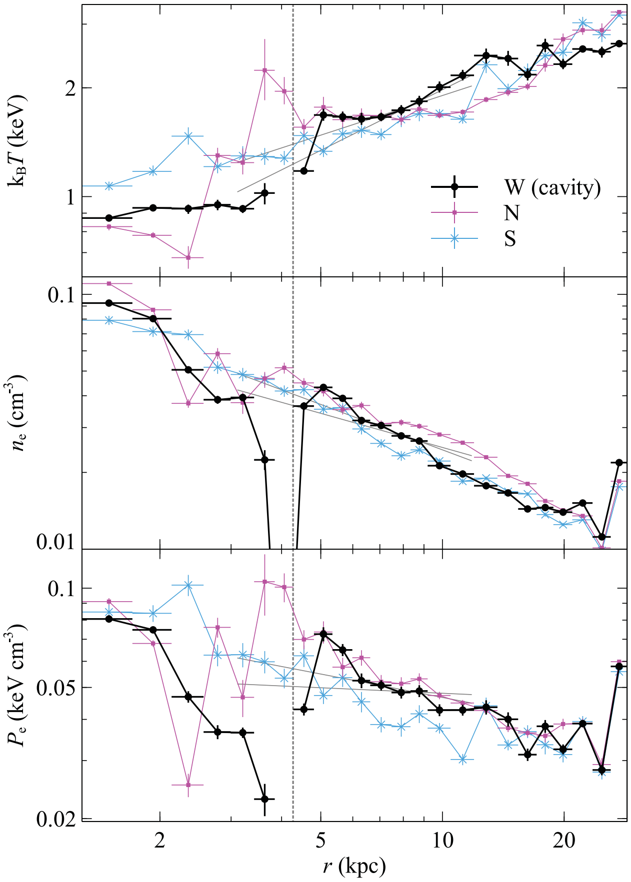

Figure 17. Deprojected temperature, density and pressure profiles across the western inner cavity and two neighbouring sectors (see Appendix A6). The cavity outer edge radius is shown by a vertical dashed line. The straight lines are two separate fits to the western points between 6–9 and 7.5–9 kpc.

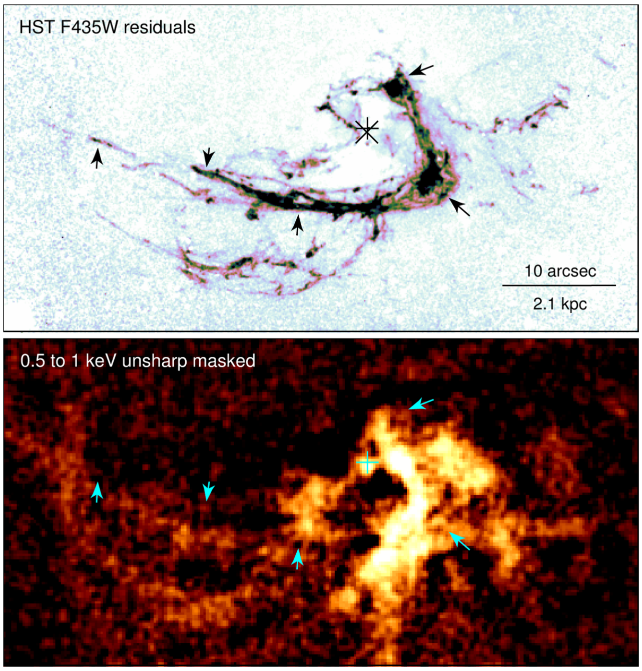

Figure 18. Central dust lanes and soft X-ray comparison. Top panel: fractional residuals of a symmetric elliptical model fitted to an *HST F435W* image of NGC 4696 from Hubble legacy data set HST_9427_06_ACS_WFC_F435W. Bottom panel: unsharp-masked 0.5–1 keV image. The arrows are in the same location in each image. '×' marks the radio nucleus, while '+' indicates the optical model centroid.

which has risen in that direction, dragging out cold material behind it (Crawford et al. 2005).

If the plume was generated by a rising bubble, which bubble is responsible? Around four-fifths of the way along the plume is an SB edge (marked as inner edge in Fig. 11) which appears to cross the plume and perhaps connects to the eastmost filament. This edge is made up of a lower temperature material, appearing to bound a cocoon-like structure (see the temperature and normalization ratio maps in Fig. 13 and the 1 keV map in Fig. 20). Inside this edge is a depression (labelled C in Fig. 13), where the majority of the extended radio emission to the north lies (Fig. 16). This could be the responsible bubble, although this does not explain why the plume extends beyond the edge towards the north-east, where it rapidly ends. There is no evidence for any other cavities or radio emission beyond the plume. It could be that the plume is not on the plane of the sky, but has a large component along the line of sight.

The similarity of the plume and the sloshing morphology could be due to its shape being affected by the motions in the ICM caused by the sloshing, giving the bend at its south. ICM motions may have also helped displace the bubble to the north, helping to drag out colder material behind it. This may also explain why there is no similar plume to the south. However, cavity E, which is associated with low-frequency radio emission, is in the opposite direction from the plume and is a plausible counterpart, albeit without the associated plume structure. Sloshing or displacement of material by buoyant bubbles may be the origin of the offset of the coldest X-ray material from the nucleus (Fig. 12). The coolest X-ray emitting material is coincident with the central dust lane (Fig. 18), which is offset from the X-ray, optical and radio nuclei.

The location of the bay (D) in the hot spiral-shaped region diagonally on the opposite side of the cool spiral-shaped plume (Fig. 13), suggests that it may be generated by the sloshing motion. The edges of the bay, however, curve in the opposite direction to the hot inward spiral. The bay also does not spiral north and inward as the temperature does, but there is an edge in SB and density to the north (Figs 1 and 13). Low-frequency radio emission is also associated with the bay region (Fig. 16). Therefore it is likely that the bay is an AGN-generated cavity and is not generated by gas sloshing in the potential well.

3.8 RM and magnetic fields

Fig. 19 shows the 9 GHz RM map, plotting contours from the intensity (top panel), soft X-rays edges (centre panel) and optical dust lane (bottom panel). Five regions with high RMs (more negative than $-1500\,\mathrm{rad\,m^{-2}}$) are identified by arrows (also shown in Fig. 15). These include the nucleus (RM3), a 850-pc-long tube-like structure which extends south-east from the nucleus (RM6) and a large gradient in RM across the western half of the source (RM2). The regions of high RM (marked by the arrows) correspond to where the X-ray emission is bright, though there is not an exact one-to-one correspondence between RM and soft X-ray emission.

We also compare the RM map with contours showing the dust lane in the centre of NGC 4696. The region in which the radio polarization can be measured is anticoincident with the strongest dust absorption regions. However, several of the regions with high RMs (RM1, RM4, RM5 and RM6) coincide with locations of dust absorption.

The RM shows a number of regions with large negative ($<-1500\,\mathrm{rad\,m^{-2}}$) values. The value of the RM is given by

$$\mathrm{RM} = 812 \int_0^L n_\mathrm{e}\, B_\parallel\, \mathrm{d}l \ \mathrm{rad\,m^{-2}}, \qquad (1)$$

where n_e is the electron density in $\mathrm{cm^{-3}}$, $B_\parallel$ is the component of the magnetic field along the line of sight in µG and the integral is over length L in kpc. In PKS 1246−410 the plausible explanations for high RM are the optical line-emitting filaments crossing in front of the radio lobes and filamentary soft X-ray emitting gas (Taylor et al. 2007) or local interactions with the synchrotron-emitting plasma (Rudnick & Blundell 2003).

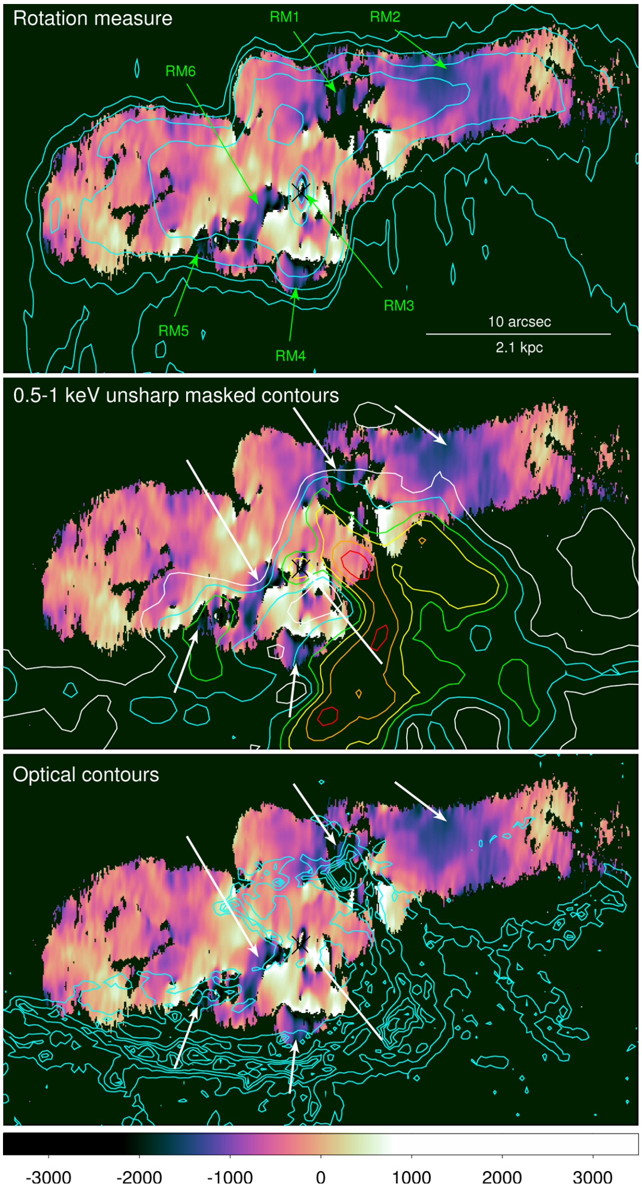

Figure 19. RM image, with radio (top), soft X-ray edges (centre) and optical (bottom) contours. The map has 1.06 × 0.26 arcsec resolution and a scale in $\mathrm{rad\,m^{-2}}$. The arrows mark five regions with RMs $<-1500\,\mathrm{rad\,m^{-2}}$. The RM varies between -3500 and $3500\,\mathrm{rad\,m^{-2}}$, with a mean of $-391\,\mathrm{rad\,m^{-2}}$ and a full width half-maximum of $668\,\mathrm{rad\,m^{-2}}$. Regions where the polarization angle uncertainty exceeds 35° are excluded. The X-ray contours come from an unsharp-masked 0.5–1 keV image and the optical show the dust lane (Fig. 18).

Several of the high- RM locations, both in the positive and negative directions, are coincident with filaments of soft X-ray emission. The tube of high negative RM south and east of the nucleus (RM6) is coincident with a soft X-ray filament, although the filament does not run along the full length of the tube but passes into a neighbouring region of high positive RM. There is, however, not an exact correspondence between the soft X-ray emission and regions of high

RM, perhaps due to surface effects in the skin of the radio source (Rudnick & Blundell 2003), or because of absorption of X-rays by the dust lane (see Section 3.6). Where the X-ray emission is brightest, along the ridge south and west of the nucleus, the polarization cannot be measured.

The lack of RM measurements in regions coincident with the soft X-ray emission and dust lane may be due to depolarization of the source. Depolarization is consistent with the gas surrounding the filaments being cooler and denser and more highly magnetized. The fields could help support the filaments, as in the Perseus cluster (Fabian et al. 2008). Depolarization is also supported by the isolated knots of high-RM signal inside regions where the polarization cannot be measured (e.g. RM1 and RM5). If the regions containing large RMs are dominated by line-emitting gas with their associated soft X-ray filaments, and magnetic support is important as in Perseus, the high RMs are likely more sensitive to the magnetic field in the filaments than those in the bulk of the ICM.

4 INNER MULTIPHASE STRUCTURE

4.1 Multiple temperature components

Examining the thermodynamic state of the central region of the cluster is important for understanding the balance between heating and cooling and on what physical scales that is occurring. A useful technique for visualizing the location of X-ray material at different temperatures is to fit a model made up of several fixed temperature components, allowing the normalization of each component to vary (Fabian et al. 2006). Fig. 20 shows the spatial distribution of the three coldest components in a model made up of 0.5, 1, 2 and 4 keV temperatures. The 0.5 keV material lies along the regions of soft X-ray emission and has a similar morphology to the dust and Hα emission (Fig. 18) and is offset from the nucleus. The 1 keV gas traces the central ridge of bright X-ray emission, the hook and the plume. The material closest to 2 keV appears associated with the rims of the inner cavities, the plume and the 'inner edge' (Fig. 11).

The core of the cluster has phases with different temperatures which are coincident in position. We examined these temperatures using a two-component variable temperature model. Fig. 21 compares a single-component map against the lower and upper temperatures of a two-temperature model, when the temperatures of the model can be constrained. Further details and results are given in Appendix B. The results show that the two components are required over the plume region (as found previously in Sanders & Fabian 2002) and in the opposite direction towards cavity E (Fig. 13). The lower temperature component drops from 1.5 keV at the end of the plume to ~0.7 keV in the regions associated with the filaments and the coldest material from the fixed component analysis (Fig. 20). The upper component has a fairly flat 2 keV temperature distribution over much of the inner region. Its temperature, however, increases to 3 keV at the end of the plume and drops to 1.3 keV in a few locations where the coolest component is lowest.

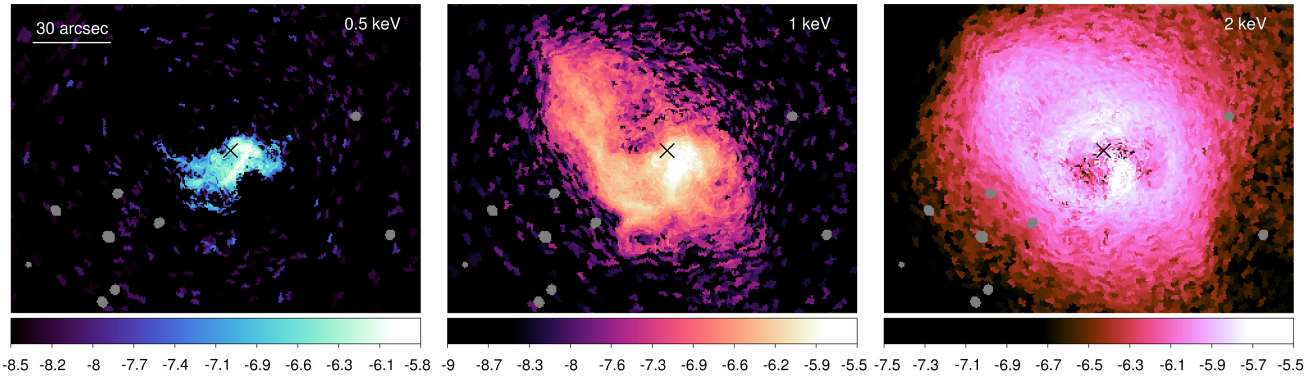

Figure 20. Normalization per unit area for components with temperatures of 0.5, 1 and 2 keV. A model was fitted with 0.5, 1, 2 and 4 keV components with $1.2\,\mathrm{Z}_{\odot}$ metallicity, using $S/N = 20$ bins, minimizing the C-statistic of the fit. The units are $\log_{10}\,\mathrm{cm}^{-5}\,\mathrm{arcsec}^{-2}$.

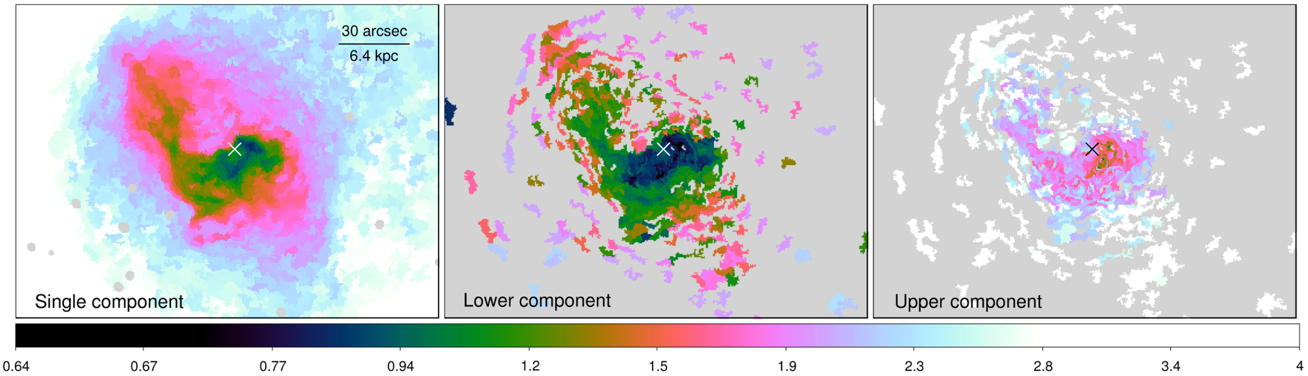

Figure 21. Comparison between the temperature (in keV) using a single-component model (left) and a two-component model (centre and right) using $S/N = 40$ bins, allowing the metallicity to vary (assuming both components have the same metallicity) and minimizing the C-statistic. Values for the two-component model are only shown when the improvement in C-statistic has 1 per cent probability of chance occurrence (determined from fits of realizations of single component models).

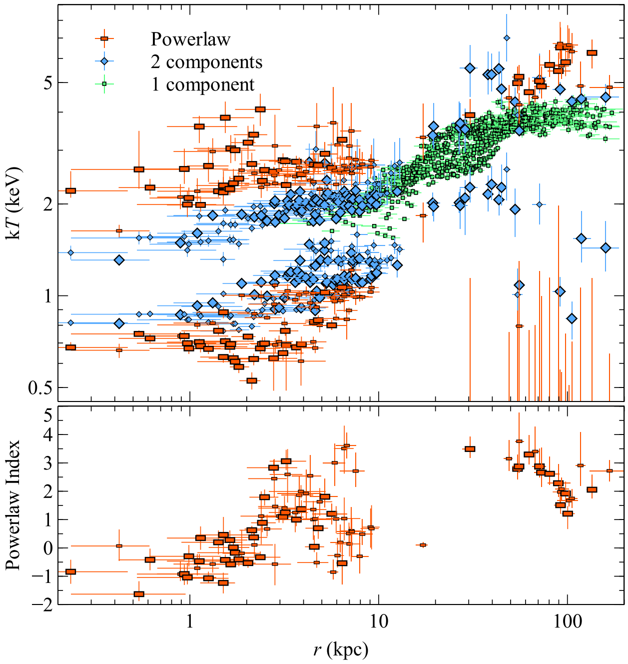

Figure 22. Power law, two or single-component fits to bins with S/N = 100. Top panel: radial temperature profiles. Power law upper and lower temperatures are shown if the upper can be determined to better than 1 keV and the index to at least 1. Two component results are shown if the temperatures can be determined to at least 20 per cent and the minimum temperature is >0.4 keV. The single component results are shown if neither of these criteria are passed. Larger markers are shown for the power law or two-component results depending on which has the lower C-statistic value. Bottom panel: the power law index parameter when appropriate.

4.2 Power-law spectral fits

In order to see whether a continuous temperature distribution is more realistic, we fitted a power-law-temperature-distribution model, which assumes that the gas has a range in temperature between T_{upper} and T_{lower}. The model is constructed using N logarithmically spaced temperature components (here 16), where the relative normalization of one component at temperature T is given by $(T/T_{\mathrm{lower}})^{\Gamma}$. Each component is assumed to have the same metallicity. This power-law model has the same number of free parameters as a two-component model, as the free normalization is substituted for the power-law index.

A comparison between the temperature values obtained with the two-component model and the power law upper and lower temperatures is shown in Fig. 22. Well-constrained temperatures and power-law indices for the two-component and power-law fits are mostly found in the central region. The obtained temperature range is wider when a power-law temperature distribution is assumed. As the two-temperature and power-law models are distinct, we cannot compare them with an F-test. However, the power-law model produces better fits in the central regions compared to the two-component model. In addition, the power-law index increases from negative values (where low temperatures dominate) to positive values (where high temperatures dominate) as a function of radius.

4.3 Accounting for projection effects

Some of the multiple components may be due to projected spectra of material along the line of sight. We therefore construct profiles from deprojected spectra in east and west sectors (Fig. 23). The eastern side of the cluster centre is strongly affected by the plume which we do not remove. The maximum difference in temperature between the eastern and western sides is around 30 per cent. Excluding the cavities, the density can differ by 40 per cent. In pressure there is generally little difference between the two sides, except at the locations of the cavities (between 2.4 and 4.3 kpc radius). The single-component metallicity values show a large discrepancy between the east and west, although when two temperature components are used, this difference becomes much smaller.

We can also fit the power-law distribution model to the deprojected data. The results of these fits (Fig. 24) show a similar trend to the projected results, where the power-law temperature range is wider than the two temperatures of the two-component fits. The index cannot be constrained very well, but scatters around a value of 0. If we examine the best-fitting metallicity for the single-component, two-component and power-law deprojected fits and the two-component projected fits, then we find that there is reasonable agreement for all these models except for the single-component deprojected results, which show a stronger drop in metallicity in the central regions. However, all the results show a central metallicity drop. In the figure we also plot the χ^2 of the best fit to the deprojected spectra for each of the models. The two-component and power-law models fit the data better in the central regions, but there is little difference in the fit quality between these two models there. In the projected fits, the power-law model appeared to fit the data better than the two-component model in the central regions, but it is unclear whether this is due to projection effects or data quality.

4.4 Discussion

There is projected emission down to ∼0.9 keV with a single-component model or 0.7 keV with two components. This is roughly consistent with the *XMM*–RGS results (Sanders et al. 2008) which show Fe XVII emission, with material down at 0.3−0.45 keV. The difference may be due to projection effects, the limited spectral resolution of ACIS and the assumption of $1.2 \times 10^{21}\ \mathrm{cm}^{-2}$ absorbing hydrogen column density in this analysis. There is dust associated with the filaments which could contain additional absorbing material. We also note that we always assume that the thermal components have the same metallicity, which may not be the case.

The coolest X-ray filaments lie closest to the core of the cluster at the location of the dust filaments, albeit with an offset (Figs 18 and 12). The X-ray gas is clearly multiphase in the centre of the cluster and more than one thermal component is required to fit the spectra (e.g. Fig. 24). The multiphaseness is not due to projection effects caused by the cluster temperature gradient and is seen in deprojected spectra (Fig. 23). Introducing two components into the spectral model (Fig. B1) shows that there is a 0.8–2 keV temperature range over most of the inner 6 kpc, rather than the more smoothly varying profile as seen in the one-component model. Note that two components are only required in the plume beyond this radius. The two-component model decreases the minimum temperature found in the region, but the change is not dramatic (likely due to the fine spatial binning used here). As there is a similar range in temperatures seen using a two-component compared to a single-component model within the inner 10 kpc, this suggests that the multiphase filamentary structures we observe on the sky are replicated along the line of sight in this region.

Despite the lack of a much wider range in temperatures, we do observe slightly cooler gas down to 0.7 keV in the core when using two temperature models. The multitemperature structure is

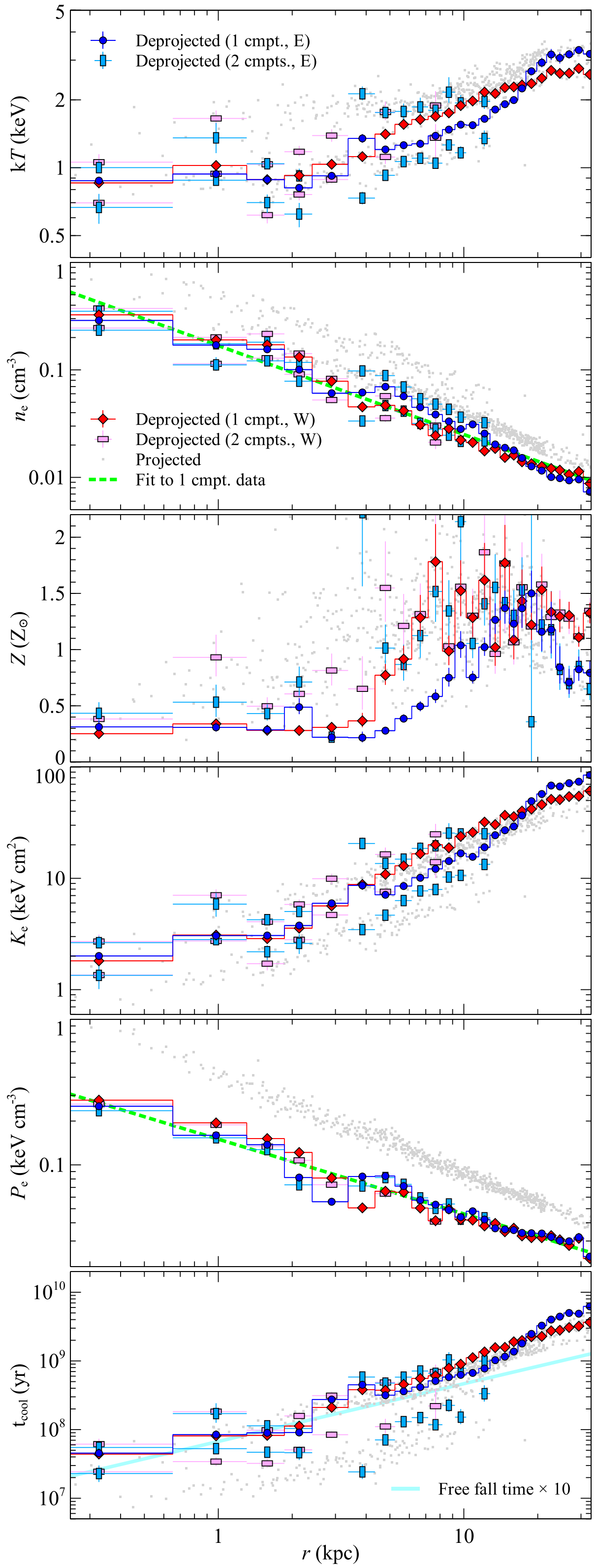

Figure 23. Deprojected profiles for the eastern (E) and western halves (W) of the cluster. Shown are the results for single- and two-component models (where the errors on the temperatures are less than 20 per cent). See Appendix A7 for details. We plot the results from projected two-temperature fits for comparison (Appendix B; plotting every fourth point). Power-law fits to the pressure and density profiles, and the estimated free fall time, are shown.

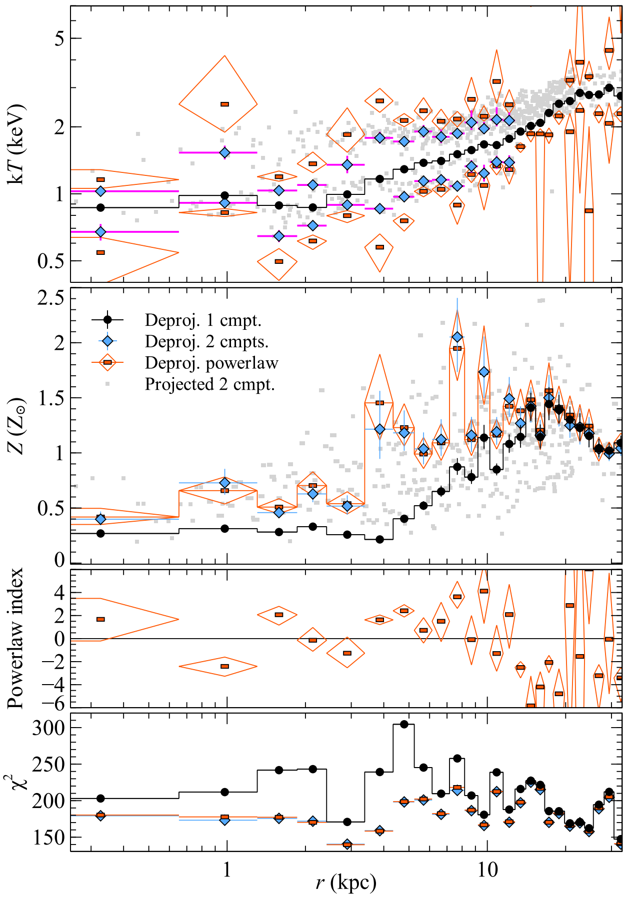

Figure 24. Comparison of power-law, single and two-component model deprojected spectral fits. Panels are the temperature (top), metallicity (second), power law index (third) and fit χ^2 (bottom). The projected two-component results are also shown, plotting only every fourth point.

associated with the filaments and plume and appear suddenly within a radius of 10 kpc. There is in addition evidence for a wider range of temperatures when fitting models with a power-law temperature distribution (Fig. 22). Power-law models provide increasingly good fits to the data compared to two-component models going to smaller radii. The index of the power law also significantly decreases at a smaller radius, indicating there is relatively more gas at lower temperatures. The minimum temperature in the power-law distribution tends to drop down to ∼0.5 keV, close to the *XMM* results. Similar power-law distribution fits are also supported when projection effects are removed (Fig. 24), although no improvement in the spectral fit over a two-component model is seen in this case. The two-temperature models give a range in temperature of a factor of ∼2 in the core, which increases to ∼4 with power-law models. The multicomponent maps of the cluster core similarly give a range of ∼4 in the core of the cluster (Fig. 20).

The minimum temperature of the single-component, two-component and power-law models decreases roughly with radius, although the coldest X-ray gas is offset from the nucleus and X-ray centroid (Fig. 12). We note that the X-ray filaments in Centaurus are coolest, densest and better defined closer towards the nucleus (e.g. Figs 11, 12 and 20). Dust filaments appear to extend down to the radio nucleus, however (Fig. 18). If the shell at the centre of the cluster is a shock, they must survive it. Given the structure on small scales, it is difficult to define the centre and account for projection.

Instead of the cool filaments being pulled out from the central galaxy by rising bubbles, it has been suggested that cold blobs could condense out of the ICM when the ratio of the cooling to the free-fall time-scale drops too low (Gaspari, Ruszkowski & Sharma 2012; McCourt, Quataert & Parrish 2013; Li et al. 2015). We can estimate free-fall time-scale for the cluster from the X-ray data. At a radius r the free-fall time-scale is given by $t_{\rm ff} = (2r/g)^{1/2}$. The gravitational acceleration, g, if the cluster is in hydrostatic equilibrium is given by $g = -(1/\rho)\,\mathrm{d}P/\mathrm{d}r$, where P is the total pressure and ρ is the mass density. The electron pressure in the cluster is approximated by a power-law model (Fig. 23), $P_{\rm e} = 0.150(r/\mathrm{kpc})^{-0.51}\,\mathrm{keV\,cm^{-3}}$, while the electron density is approximated by $n_{\rm e} = 0.168(r/\mathrm{kpc})^{-0.83}\,\mathrm{cm^{-3}}$. Therefore the gravitational acceleration in the centre of the cluster is $\sim 1.4 \times 10^{-7}(r/\mathrm{kpc})^{-0.68}\,\mathrm{cm\,s^{-2}}$. The implied free-fall time closely tracks a 10th of the cooling time (Fig. 23). It is not obvious from the data for this model why there should be multiphase gas within a certain radius given that there is not a large variation in the ratio of cooling and free-fall times.

We note that the only multiphase gas present beyond 6 kpc radius is in the plume and other related cool structures (Fig. 21). There is low-frequency radio emission associated with the plume, showing it is likely material which has been dragged out by a rising cavity. There are no cool blobs of material outside the plume region beyond 6 kpc radius which would indicate general condensation at larger radius where the cooling time is 10 times the free-fall time.

5 CENTRAL ABUNDANCE DROP

Previous work has shown a central drop in abundance in the cluster (Sanders & Fabian 2002; Panagoulia et al. 2013). Here we examine this on small spatial scales using these new deeper data. The deprojected metallicity profiles of different elements to the east and west of the cluster core are shown in Fig. 25. We note, however, that this analysis assumes that the phases in each radial bin have the same metallicity, which may not be a valid assumption. CCD-quality data are not good enough to test this assumption. To the eastern side of the cluster the metallicities appear to exhibit more bin-to-bin variation than the west. This is also seen in metallicity profiles with finer bins (Fig. 23). This could be real, however it may be due to incorrect modelling of the complex thermal structure in the plume or it may be because the assumption of spherical symmetry when deprojecting is invalid.

The profiles are consistent with central reductions in many of the probed elemental abundances (Fe, Si, S, Mg and O). In the other metals, it is unclear whether the profiles are flat or declining, due to large measurement uncertainties or differences between the two modelling approaches. We note that several of the elemental lines are not clearly separated in these CCD spectra (e.g. Ni and Ne lines are close to the strong Fe-L lines) and therefore they cannot be measured unambiguously. Furthermore, the O abundance is affected by the choice of the absorbing column density.

We therefore confirm the central drop in metallicity in the cluster. Panagoulia et al. (2013) suggests that the metals are locked into dust in the centre of the cluster, they are moved to larger radius by feedback processes, the grains are destroyed (e.g. by sputtering) and the metals returned to the hot phase. Such a scenario could also explain the metallicity blobs and flat inner metallicity profile (Section 2.6). Fig. 25 is consistent with this picture, confirming that Fe, Si and S abundances drop in the centre to around a third of their peak value. Furthermore, we also find evidence for Mg and O depletion, although these metallicities have some modelling uncertainties. These are all metals which can form part of dust. Unfortunately, the quality of the data is insufficient to measure the central Ar abundance, which is unlikely be depleted by dust formation. With the aid of detailed models of dust composition it may be possible in the future to test the dust deposition model in Centaurus using those elements which we can measure.

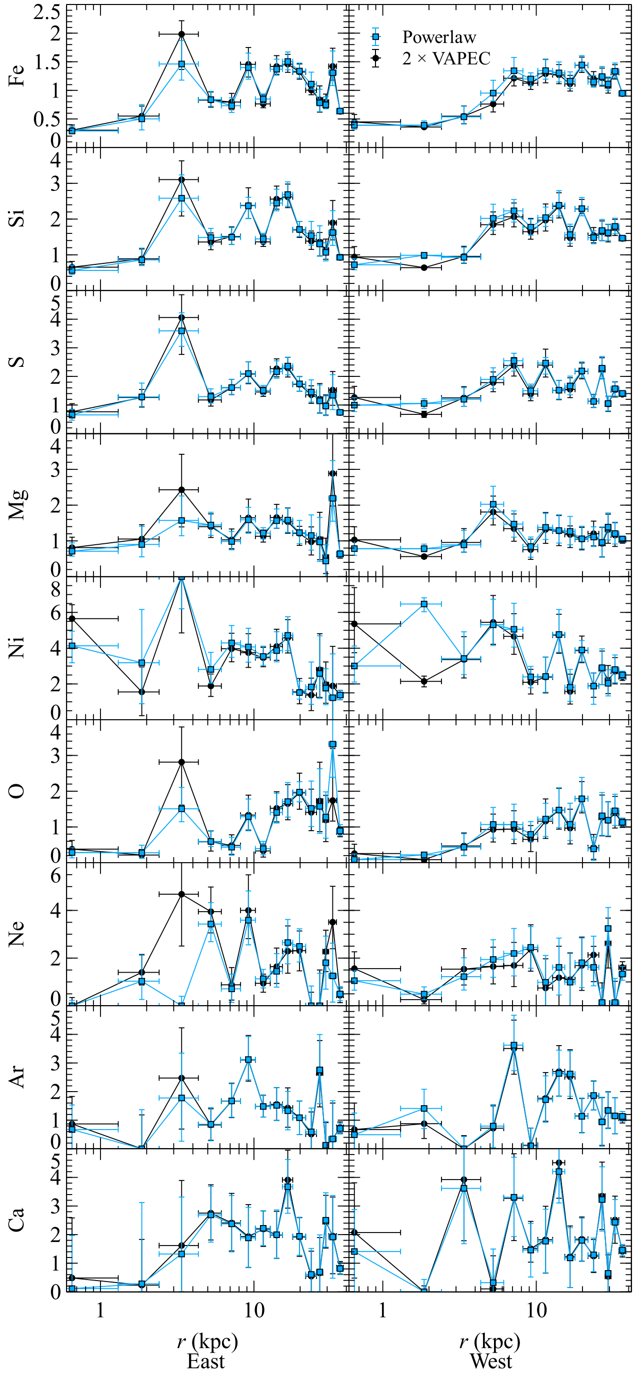

Figure 25. Elemental abundances (in solar units) to the east and west of the cluster core, obtained by fitting two-component or power-law distribution VAPEC models to deprojected spectra. Analysis details are given in Appendix A8.

Upcoming X-ray observatories such as *Athena* (Nandra et al. 2013) will make extremely precise measurements of the temperature distribution and metallicity in the core of Centaurus and those other clusters (Panagoulia et al. 2015) which show central drops in metallicity. *Athena* will also be able to measure the metallicity of different phases independently.

6 CONCLUSIONS

We analysed deep new *Chandra* observations of the Centaurus cluster, examining the larger-scale structure, metallicity distribution, cold fronts and region around the nucleus. The main conclusions of our paper are as follows.

(i) Gradient filtering using the GGM filter is able to robustly reveal previously hard-to-discern structures in X-ray images of galaxy clusters.

(ii) The correlation on larger scales of the metals with SB and inverse correlation with temperature implies that the asymmetry in the cluster is dominated by sloshing motions.

(iii) Enriched dusty material, uplifted by AGN activity would simultaneously explain the low inner metallicities, the flat inner metallicity profile in the core and the existence of 5–10 kpc high metallicity blobs on the western side of the cluster.

(iv) We find 7 kpc 'notches' around the edge of the western cold front which may be KHIs. There are strong point-to-point changes in the sharpness of the cold front on 10° scales. In some sectors the width of the edge is less than or equal to the electron mean free path.

(v) We identify a 1.9-kpc-radius shell around the nucleus. This could be a shock generated by an AGN outburst $\lesssim$3.5 Myr ago. A shock may also explain why the coldest X-ray gas is offset from the nucleus, though this could also be due to sloshing motions in the cluster. A significant fraction of energy in bubbles has already passed into ICM in the form of a higher pressure region.

(vi) Around the western cavity and to the north is a weak shock seen in temperature, density and pressure. To the western side the implied Mach numbers are between 1.1 and 1.4, while they are higher to the north (1.6 to 2.2).

(vii) There are $\sim$9 depressions in X-ray SB around the core of the cluster, some of which may be associated with radio emission. The shock and multiple bubbles suggests that the nucleus is rapidly active on 5–10 Myr time-scales.

(viii) We confirm the existence of a quasi-periodic set of SB variations, which we previously claimed could be sound waves. The spacing of the peaks of $\sim$5 kpc would imply a period of 6 Myr, if they are sound waves, which is similar to the ages of the shock and bubble. Alternatively, they could be generated by the sloshing, consisting of projected KHIs and their associated turbulence, or amplified magnetic field regions.

(ix) Around the nucleus there is filamentary multiphase X-ray gas. As found previously, it is spatially correlated with material at lower temperatures. Fitting data with power-law temperature distributions gives better fits in the centre, implying a continuous temperature distribution over a factor of $\sim$4 in temperature.

ACKNOWLEDGEMENTS

We thank the referee E. Roediger for helpful suggestions which improved this paper. ACF, HRR and SAW acknowledge support from the ERC Advanced Grant FEEDBACK. Support for this work was provided by the National Aeronautics and Space Administration through Chandra Award Numbers G01-12156X, GO2-13149X and GO4-15121X issued by the Chandra X-ray Observatory Center, which is operated by the Smithsonian Astrophysical Observatory for and on behalf of the National Aeronautics Space Administration under contract NAS8-03060. The scientific results reported in this article are based on observations made by the *Chandra X-ray Observatory* and data obtained from the Chandra Data Archive. Based on observations made with the NASA/ESA *Hubble Space Telescope*, and obtained from the Hubble Legacy Archive, which is a collaboration between the Space Telescope Science Institute (STScI/NASA), the Space Telescope European Coordinating Facility (ST-ECF/ESA) and the Canadian Astronomy Data Centre (CADC/NRC/CSA).The National Radio Astronomy Observatory is a facility of the National Science Foundation operated under cooperative agreement by Associated Universities, Inc.

REFERENCES

Allen S. W., Fabian A. C., 1994, MNRAS, 269, 409

Allen S. W., Fabian A. C., Johnstone R. M., Arnaud K. A., Nulsen P. E. J., 2001, MNRAS, 322, 589

Anders E., Grevesse N., 1989, Geochim. Cosmochim. Acta, 53, 197

Arnaud K. A., 1996, in Jacoby G. H., Barnes J., eds, ASP Conf. Ser. Vol. 101, Astronomical Data Analysis Software and Systems V. Astron. Soc. Pac., San Francisco, p. 17

Ascasibar Y., Markevitch M., 2006, ApJ, 650, 102

Balucinska-Church M., McCammon D., 1992, ApJ, 400, 699

Blanton E. L., Randall S. W., Clarke T. E., Sarazin C. L., McNamara B. R., Douglass E. M., McDonald M., 2011, ApJ, 737, 99

Canning R. E. A., Fabian A. C., Johnstone R. M., Sanders J. S., Crawford C. S., Hatch N. A., Ferland G. J., 2011a, MNRAS, 411, 411

Canning R. E. A., Fabian A. C., Johnstone R. M., Sanders J. S., Crawford C. S., Ferland G. J., Hatch N. A., 2011b, MNRAS, 417, 3080

Chatzikos M. et al., 2015, MNRAS, 446, 1234

Churazov E., Gilfanov M., Forman W., Jones C., 1999, ApJ, 520, 105

Crawford C. S., Hatch N. A., Fabian A. C., Sanders J. S., 2005, MNRAS, 363, 216

Fabian A. C., Nulsen P. E. J., Atherton P. D., Taylor K., 1982, MNRAS, 201, 17P

Fabian A. C., Sanders J. S., Allen S. W., Crawford C. S., Iwasawa K., Johnstone R. M., Schmidt R. W., Taylor G. B., 2003, MNRAS, 344, L43

Fabian A. C., Sanders J. S., Taylor G. B., Allen S. W., 2005, MNRAS, 360, L20

Fabian A. C., Sanders J. S., Taylor G. B., Allen S. W., Crawford C. S., Johnstone R. M., Iwasawa K., 2006, MNRAS, 366, 417

Fabian A. C., Johnstone R. M., Sanders J. S., Conselice C. J., Crawford C. S., Gallagher J. S., III, Zweibel E., 2008, Nature, 454, 968

Fabian A. C., Sanders J. S., Williams R. J. R., Lazarian A., Ferland G. J., Johnstone R. M., 2011, MNRAS, 417, 172

Ferland G. J., Fabian A. C., Hatch N. A., Johnstone R. M., Porter R. L., van Hoof P. A. M., Williams R. J. R., 2009, MNRAS, 392, 1475

Foreman-Mackey D., Hogg D. W., Lang D., Goodman J., 2013, PASP, 125, 306

Forman W. et al., 2007, ApJ, 665, 1057

Fruscione A. et al., 2006, in Silva D. R., Doxsey R. E., eds, Proc. SPIE Conf. Ser. Vol. 6270, Observatory Operations: Strategies, Processes, and Systems. SPIE, Bellingham, p. 62701V

Fukazawa Y., Ohashi T., Fabian A. C., Canizares C. R., Ikebe Y., Makishima K., Mushotzky R. F., Yamashita K., 1994, PASJ, 46, L55

Gaspari M., Ruszkowski M., Sharma P., 2012, ApJ, 746, 94

Goodman J., Weare J., 2010, Commun. Appl. Math. Comput. Sci., 5, 65

Graham J., Fabian A. C., Sanders J. S., Morris R. G., 2006, MNRAS, 368, 1369

Graham J., Fabian A. C., Sanders J. S., 2008, MNRAS, 386, 278

Grimes C. K., 2014, Master's thesis, Univ. New Mexico

Ikebe Y., Makishima K., Fukazawa Y., Tamura T., Xu H., Ohashi T., Matsushita K., 1999, ApJ, 525, 58

Johnstone R. M., Hatch N. A., Ferland G. J., Fabian A. C., Crawford C. S., Wilman R. J., 2007, MNRAS, 382, 1246

Laine S., van der Marel R. P., Lauer T. R., Postman M., O'Dea C. P., Owen F. N., 2003, AJ, 125, 478
Landau L. D., Lifshitz E. M., 1959, Fluid Mechanics. Pergamon Press, Oxford
Li Y., Bryan G. L., Ruszkowski M., Voit G. M., O'Shea B. W., Donahue M., 2015, ApJ, 811, 73
Lucey J. R., Currie M. J., Dickens R. J., 1986, MNRAS, 221, 453
McCourt M., Quataert E., Parrish I. J., 2013, MNRAS, 432, 404
Markevitch M., Vikhlinin A., 2007, Phys. Rep., 443, 1
Mittal R. et al., 2011, MNRAS, 418, 2386
Nandra K. et al., 2013, preprint (arXiv:1306.2307)
Ota N. et al., 2007, PASJ, 59, 351
Panagoulia E. K., Fabian A. C., Sanders J. S., 2013, MNRAS, 433, 3290
Panagoulia E. K., Sanders J. S., Fabian A. C., 2015, MNRAS, 447, 417
Paterno-Mahler R., Blanton E. L., Randall S. W., Clarke T. E., 2013, ApJ, 773, 114
Rafferty D. A., McNamara B. R., Nulsen P. E. J., Wise M. W., 2006, ApJ, 652, 216
Randall S. W. et al., 2015, ApJ, 805, 112
Reiprich T. H., Böhringer H., 2002, ApJ, 567, 716
Roediger E., Brüggen M., Simionescu A., Böhringer H., Churazov E., Forman W. R., 2011, MNRAS, 413, 2057
Roediger E., Lovisari L., Dupke R., Ghizzardi S., Brüggen M., Kraft R. P., Machacek M. E., 2012, MNRAS, 420, 3632
Roediger E., Kraft R. P., Forman W. R., Nulsen P. E. J., Churazov E., 2013, ApJ, 764, 60
Rudnick L., Blundell K. M., 2003, ApJ, 588, 143
Russell H. R., Sanders J. S., Fabian A. C., 2008, MNRAS, 390, 1207
Sakuma E., Ota N., Sato K., Sato T., Matsushita K., 2011, PASJ, 63, 979
Sanders J. S., 2006, MNRAS, 371, 829
Sanders J. S., Fabian A. C., 2002, MNRAS, 331, 273
Sanders J. S., Fabian A. C., 2006a, MNRAS, 370, 63
Sanders J. S., Fabian A. C., 2006b, MNRAS, 371, 1483
Sanders J. S., Fabian A. C., 2007, MNRAS, 381, 1381
Sanders J. S., Fabian A. C., 2008, MNRAS, 390, L93
Sanders J. S., Fabian A. C., Allen S. W., Morris R. G., Graham J., Johnstone R. M., 2008, MNRAS, 385, 1186
Sanders J. S., Fabian A. C., Taylor G. B., 2009a, MNRAS, 393, 71
Sanders J. S., Fabian A. C., Taylor G. B., 2009b, MNRAS, 396, 1449
Shobbrook R. R., 1963, The Observatory, 83, 36
Simionescu A. et al., 2012, ApJ, 757, 182
Smith R. K., Brickhouse N. S., Liedahl D. A., Raymond J. C., 2001, ApJ, 556, L91
Sparks W. B., Macchetto F., Golombek D., 1989, ApJ, 345, 153
Taylor G. B., Fabian A. C., Allen S. W., 2002, MNRAS, 334, 769
Taylor G. B., Sanders J. S., Fabian A. C., Allen S. W., 2006, MNRAS, 365, 705
Taylor G. B., Fabian A. C., Gentile G., Allen S. W., Crawford C., Sanders J. S., 2007, MNRAS, 382, 67
Walker S. A., Fabian A. C., Sanders J. S., 2013, MNRAS, 435, 3221
Walker S. A., Fabian A. C., Kosec P., 2014, MNRAS, 445, 3444
Walker S. A., Sanders J. S., Fabian A. C., 2015, MNRAS, 453, 3699
Werner N. et al., 2016, MNRAS, 455, 846
ZuHone J. A., Markevitch M., Lee D., 2011, ApJ, 743, 16
ZuHone J. A., Kunz M. W., Markevitch M., Stone J. M., Biffi V., 2015, ApJ, 798, 90

APPENDIX A: DATA ANALYSIS

A1 Initial processing

The *Chandra* Advanced CCD Imaging Spectrometer (ACIS-S) observations listed in Table A1 are examined in this paper. Data set 504 was first presented in Sanders & Fabian (2002) and observations 5310, 4954 and 4955 were first examined in Fabian et al. (2005). The data sets were reprocessed with CIAO version 4.6 (Fruscione et al. 2006). Bad time periods were identified by examining the light curve on the ACIS-S1 CCD with 200 s bins, clipping bins which deviated from the standard deviation by more than 2.5σ, assuming Poisson errors. We excluded data from ACIS CCDs other than 6, 7 and 8 from our observations. For each input data set, we created background data sets using standard blank-sky background files. For each CCD and observation, we took the appropriate background event file and removed events which occurred in bad pixels of their respective observation. The backgrounds were then reprojected to match the observation coordinates and attitude and their exposure times were changed to match the foreground count rate in the 9–12 keV band. In order to make total foreground and total background spectra, it was necessary to make the ratio of each background to the total background exposure time be the same as the ratio of the respective foreground to the total foreground exposure. To do this, we reduced the exposure time keywords of background event files where this was not the case, discarding random X-ray events in order to preserve the count rate. Before analysis, the foreground and background event files were reprojected to the coordinate system of the 16 223 observation.

Table A1. *Chandra* observation identifiers (OBSIDs) analysed. Listed are the observation date, the full exposure time and the exposure after cleaning.

OBSID	Date	Full (ks)	Cleaned (ks)
504	2000-05-22	31.8	26.0
505	2000-06-08	10.0	10.0
4190	2003-04-18	34.3	34.1
4191	2003-04-18	34.0	33.8
4954	2004-04-01	89.1	85.4
4955	2004-04-02	44.7	43.1
5310	2004-04-04	49.3	48.7
16223	2014-05-26	179.0	176.2
16224	2014-04-09	42.3	41.2
16225	2014-04-26	30.1	29.7
16534	2014-06-05	55.4	55.0
16607	2014-04-12	45.7	44.6
16608	2014-04-07	34.1	33.3
16609	2014-05-04	82.3	81.7
16610	2014-04-27	17.3	17.1
Total		779.3	760.0

Unless otherwise specified, spectra were fitted between 0.5 and 7 keV in XSPEC (Arnaud 1996) 12.8.2 using an APEC 2.0.2 thermal model (Smith et al. 2001). We assume the relative solar abundances of Anders & Grevesse (1989). Note that the APEC model fitted here was not the standard one, but was recomputed to have temperature steps of 0.01 dex, rather than 0.1 dex, as the steps were otherwise visible in radial plots of the temperature. Galactic absorption was modelled using a PHABS model (Balucinska-Church & McCammon 1992), with an equivalent hydrogen column of 1.2×10^{21} cm^{-2}, the average of the central region if the column is allowed to be free (note that this is not a good choice for the region of the edge-on disc galaxy which contains absorbing material, leading to incorrect results there). All deprojected profiles were calculated by fitting spectra deprojected using the DSDEPROJ method (Sanders & Fabian 2007; Russell, Sanders & Fabian 2008).

Exposure maps were created using MKEXPMAP, assuming a 3.6 keV spectrum with 0.7 $Z_\odot$ metallicity and Galactic absorption. When creating images of the larger regions, we masked the edges of the CCDs before adding to remove residuals.

A2 Large-scale spectral mapping procedure

We used the Contour Binning algorithm (Sanders 2006) to select regions with a minimum signal to noise ratio threshold (S/N). The algorithm chooses bins which follow contours of SB, usually on an adaptively smoothed image. Bins are grown pixel by pixel until the threshold is reached. A geometric constraint factor, C, is also applied, where a pixel is not added if its radius from the bin centroid is more than C times the radius of a circle with the same area as the bin. This constraint prevents bins becoming too elongated.

We examined spectra with an S/N = 100 (i.e. 10^4 counts for regions where the background is not significant). The input smoothed image was an adaptively smoothed image, created using a kernel with a minimum signal to noise ratio of 60 in the 0.5 to 7 keV band. A geometric constraint of $C = 2$ was used in the binning. We masked out point sources in the X-ray image (see Section 2.1).

For each of the bins, each of the CCDs and each of the data sets we extracted foreground and background spectra and created response and ancillary response files. We added the foreground spectra from the observations for each of the bins for each CCD. The background spectra were similarly summed. Spectra were grouped to have at least 8 counts per spectral bin. The response and ancillary responses were spatially weighted by the number of counts in the 0.5–7 keV band. For each bin and each CCD we averaged the responses, weighting by the number of counts in the respective foreground spectrum. The spectra and responses for the different CCDs were not added to avoid combining data with distinct responses.

When fitting we minimized the C-stat fit statistic. If a bin had spectra from more than one CCD, they were fitted simultaneously with additional free parameters to account for the difference in normalization due to geometry and detector differences.

There are regions, particularly close to the nucleus, where two temperature components are necessary to fit the spectra. At the temperatures seen in Centaurus, two-component modelling is usually required if a single component is too narrow to fit the Fe-L complex, indicating that there are comparable emitting components along the line of sight which differ significantly in temperature. We discuss this in more detail in Section 4 and also examine models with more components. We therefore also fit the spectra with a model with two temperature components in each bin, assuming that they both have the same metallicity (it is not possible to fit for the metallicities of the components separately).

It is not clear what criteria should be used to decide between single- or two-component models. We investigated using the F-test and examining the size of the error bars on the best-fitting temperatures. These criteria appeared to either select two components for a number of outer regions, many with unrealistic temperatures, or did not select the two-component models in all appropriate locations in the centre, leading to a large scatter in the metallicity. The best criterion appeared to be to select two components for those regions where there was a reduction in C-stat better than 5 per cent. The resulting combined single- and two-component metallicity map appears similar to the two-component map, except for the level of scatter in regions where only one component was required.

A3 Western cold front edge

We examined deprojected spectra across the western cold front in two different sectors (Fig. A1), where the edge is clearest towards the north- and south-west, obtaining the profiles in Fig. A2. There are jumps in temperature and density (in opposite directions) by 20 per cent at the edge, leading to a continuous pressure distribution, confirming that the feature is a cold front. The entropy reduces by 25–30 per cent in the inward direction. Despite the clear correlations between the edges and metallicity (Fig. 5), we do not see the change in metallicity at the edge in the deprojected profiles.

To examine the SB profiles in detail around the edge, exposure-corrected background-subtracted profiles were extracted in the 0.5–4 keV band, with 0.492 arcsec binning between radii of 1.7 and 4.5 arcmin (Fig. A1). This band is largely sensitive to the density

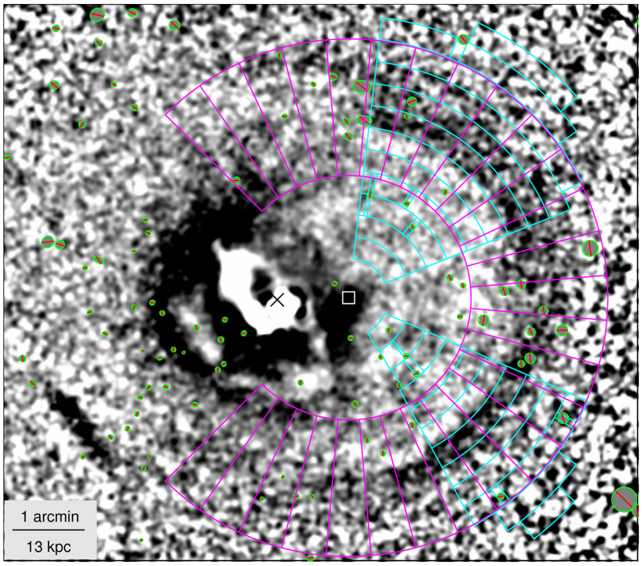

Figure A1. Regions used for examining the western cold front, shown on an unsharp-masked image. 27 sectors were used for SB extraction. Two sets of annular sectors to the north-west and south-west were used to examine the spectra. The cross marks the radio nucleus of the cluster. The box marks the centre of the annuli used, which is the same as used in Fig. 8.

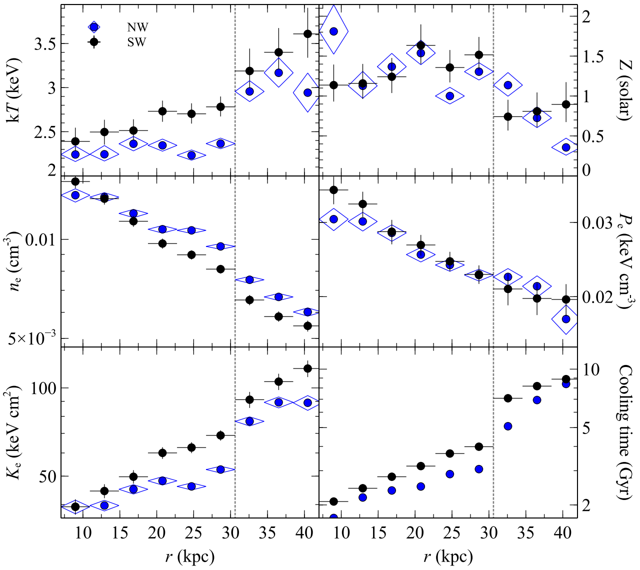

Figure A2. Deprojected thermodynamic profiles across the western cold front in the north-west and south-west directions (Fig. A1). Plotted are the temperature, metallicity, electron density, electron pressure, electron entropy and mean radiative cooling time. The vertical line marks the cold front radius. The outer three bins are not shown due to edge effects giving oscillating values.

(varying the temperature from 2.5 to 3 keV leads to a 10 per cent variation in count rate).

We took an emissivity model in which there are two power laws which jump at a particular radius. The radius of the jump, the jump ratio (the emissivity ratio outside divided by that inside), the power-law indices and the overall model normalization are free parameters. We allowed for broadening of the edge by interpolating between the two power-law models using the integral of a Gaussian with a variable σ. This emissivity profile was projected on the sky assuming spherical symmetry, integrating the emissivity profile between 1 and 7 arcmin radius in 0.246 arcsec (half pixel) steps. The model was then convolved with the PSF in the radial direction at the edge for each sector. The PSF was calculated using SAOTRACE 2.0.4 and MARX 5.1.0 assuming a 3 keV spectrum with $1.2\,\mathrm{Z}_\odot$ metallicity. The model was then resampled to have the same binning as the data.

We applied this model to the data and examined the allowed range of parameter values using the EMCEE (Foreman-Mackey et al. 2013) Markov Chain Monte Carlo (MCMC) EMCEE code, which uses an affine-invariant sampler (Goodman & Weare 2010). We force the jump radius to lie between 1.9 and 3 arcmin, the power-law indices to lie between −4 and 0.5, the jump ratio to lie between 0.01 and 2 (smaller values are larger jumps) and the Gaussian σ to be between 0.001 and 1 arcmin (the log value of σ was varied in the MCMC). In the MCMC analysis we used χ^2 likelihoods, 400 walkers, a burn in period of 1000 and a chain length of 1000. The data were fitted only inside a radius of 40 kpc, as in several sectors, particularly to the north, there is an SB break at this radius. We also investigated models which also included this break, fitting the data out to 57 kpc radius. The results from this more complex model are in reasonable agreement to those presented here. In our analysis, we found that the outer power-law index was affected by the outer integration radius. Reducing the outer radius to 6 arcmin decreases the index by 0.2–0.5. The median models and the surrounding 1σ percentiles are shown as shaded regions in Fig. A3. The parameters from the fits are plotted in Fig. 9. We also did the analysis with twice the number of sectors, finding consistent results. The radius results are plotted in Fig. 9, showing that the variation in radius seen in the 27 bin results is real.

A4 Metallicity fluctuations

Spectra from regions X and Y (Fig. 10) were extracted and fitted with single and two-component VAPEC thermal models (connecting the metallicity between the two components). Some of the emission in the regions could come from projected cluster emission. To attempt to account for this, we extracted a background spectrum from an adjacent part of the cluster outside the bright western region. We fit the spectra using this background and secondly using a standard blank-sky background spectrum, between 0.5 and 8 keV. As the two-component model temperatures were not always well constrained, we conducted an MCMC analysis to better explore the allowed parameter space using XSPEC_EMCEE (https://github.com/jeremysanders/xspec_emcee), applying 400 walkers, a burn-in period of 1000 and a chain length of 1000 iterations. The temperature values were assumed to lie between 0.15 and 20 keV. We allowed the O, Ne, Mg, Si, S, Ar, Ca, Fe and Ni metallicities to be free and fixed others to Solar values. The error bar shows the 1σ percentiles from the chain, while the point shows the median.

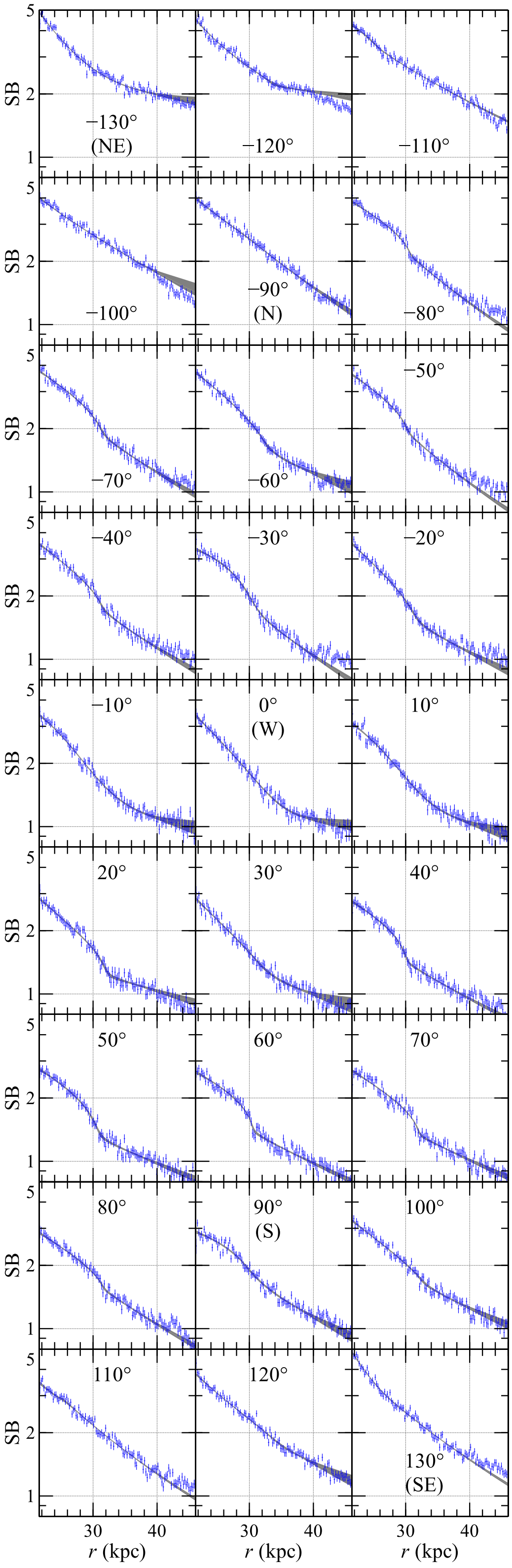

Figure A3. SB profiles in the 0.5–4 keV band across the western cold front in 27 10° sectors (depicted in Fig. A1) from the north-east (top left) through west to the south-east (bottom right) in 0.984 arcsec bins. The 0.492-arcsec-binned profiles were fitted within 40 kpc by a model in which the emissivity is a power law which jumps to a second power law at some radius, with the edge broadened by a Gaussian. The solid area shows the 1σ model uncertainties.

A5 Central spectral maps

We constructed detailed thermodynamic maps of the central region (Fig. 13) using $S/N = 20$ spatial bins (i.e. 400 counts where the background is not significant). The mapping was based on an adaptively smoothed image using a kernel with a minimum signal to noise ratio of 30 and applying a geometric constraint of $C = 3$, only examining a central 4.2×4.2 arcmin (54×54 kpc) box. We extracted spectra from the background observations using this box. These background spectra for each observation were also added, first artificially lowering the exposure of background spectra (discarding events and reducing exposure time correspondingly) so that the ratio of each background to the total was the same as the respective foreground observation to total. We used a central response and ancillary response matrix for all regions examined. We note that the XSPEC normalization is proportional to the emission measure and defined in XSPEC to be $10^{-14} \int n_{\mathrm{e}} n_{\mathrm{H}} \mathrm{d}V / (4\pi D_{\mathrm{A}}^2 [1+z]^2)$, where the cluster lies at a redshift z and angular diameter distance of D_{A} cm, the electron and hydrogen densities are n_{e} and n_{H} cm^{-3}, respectively and are integrated over a volume V cm^3.

Note that the assumption of constant absorbing column density where there are dust lanes in the centre of NGC 4696 is likely to be invalid. The metallicity was fixed to $1.2\,\mathrm{Z}_{\odot}$, an average value for the central region excluding where multicomponent models are preferred. Fixing the metallicity allows us to fit single-temperature models to the data where multitemperature models may be required (see Section 4), obtaining average projected temperatures and normalizations which are not biased by unrealistic best-fitting metallicities.

A6 Inner cavity profiles

We extracted deprojected spectra in annuli from a sector outwards from the western inner cavity (labelled B in Fig. 13). To better match the morphology of the inner region, we chose a centre which is that of a circle which circumscribes the outer edges of the two inner cavities (A and B). For comparison we also examine sectors to the north and south, avoiding the plume to the east. Fig. A4 shows the regions analysed. The spectra were fitted with single component models, with the metallicity fixed to $1.2\,\mathrm{Z}_{\odot}$.

A7 Deprojected central spectra

The spectra were extracted from 180° east and west sectors or complete annuli, excluding point sources. The centre used was the X-ray centroid of the central region, as in Appendix B. We fit both single- and two-component APEC models to the deprojected spectra (minimizing the χ^2). To fully explore the parameter space we ran an MCMC analysis on each deprojected spectrum. The two-component results are only shown in Fig. 23 if both temperatures can be constrained to 20 per cent. From the MCMC chains containing normalization, temperature and metallicity, the density, entropy, pressure and mean radiative cooling time were computed. To compute the two-component results the assumption that the components are in pressure equilibrium was made. In the plot, we also compare projected thermodynamic data points from Fig. B2.

A8 Elemental abundances

The metallicity profiles were obtained by fitting deprojected spectra, extracted from 180° sectors to the east and west. To increase the signal to noise, the radial bins used here are twice as wide in the centre as in Fig. 23. To properly account for the complex temperature distribution we used two-component and power-law VAPEC models. In our analysis Fe, Si, S, Mg, Ni, O, Ne, Ar and Ca abundances were allowed to vary. C, N and Al metallicities were tied to Fe. The same metallicities were assumed in all thermal components in a radial bin. Input spectra were fitted between 0.5 and 7 keV, minimizing the χ^2 statistic. Metallicities were allowed to vary between 0 and $8\,\mathrm{Z}_{\odot}$ and temperatures were allowed to vary between 0.1 and 20 keV. The 1σ error bars shown were calculated by varying the parameter until the minimum χ^2 increased by 1.0. An MCMC analysis produced very similar results, though we show the results from the simple analysis here.

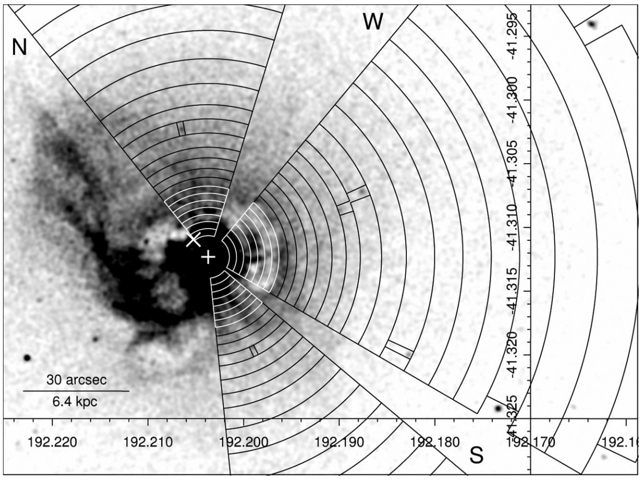

Figure A4. Regions examined to measure the ICM properties around the western inner cavity (W) and for comparison to the north (N) and south (S). The radio nucleus is marked with a '×'. The centre of the sectors is marked by a '+'. The X-ray image is unsharp-masked, subtracting 0.5 of the 0.5 to 7 keV image smoothed by 7.9 arcsec from the image smoothed by 1 arcsec.

APPENDIX B: CENTRAL THERMAL STRUCTURE

We constructed profiles of the temperature (Fig. B1) from maps with $S/N = 40$ inside 10.5 kpc radius and $S/N = 100$ at larger radii (the radius was measured from the X-ray centroid, marked in Fig. 12, at 192.204 and Dec −41.3125, not from the radio nucleus). One aspect which is different to the procedure used in Section 2.2, is that in the two-component plot the temperatures of the two-component fit are only shown if they can be constrained to better than 20 per cent, otherwise the single component result is shown. The single component fits show that the temperatures in the centre split into hotter (at high angles) and colder (at low angles) branches, where the colder branch is the cool central plume.

Although we are fitting projected spectra from regions on the sky, we can compute projected versions of the other thermodynamic properties using geometric assumptions. Here we assume that the line of sight depth of a region is the radius of the region. This assumption, which we test below, allows the normalization to be converted to a projected electron density, $n_{\mathrm{e,\,proj}}$. The electron pressure is computed as $P_{\mathrm{e,\,proj}} = n_{\mathrm{e,\,proj}}\, \mathrm{k}T$, where $\mathrm{k}T$ is the temperature in keV. The entropy is $K_{\mathrm{e,proj}} = n_{\mathrm{e,proj}}^{-2/3}\, \mathrm{k}T$. We also calculate a mean radiative cooling time $t_{\mathrm{cool,\,proj}}$ by dividing the enthalpy of a

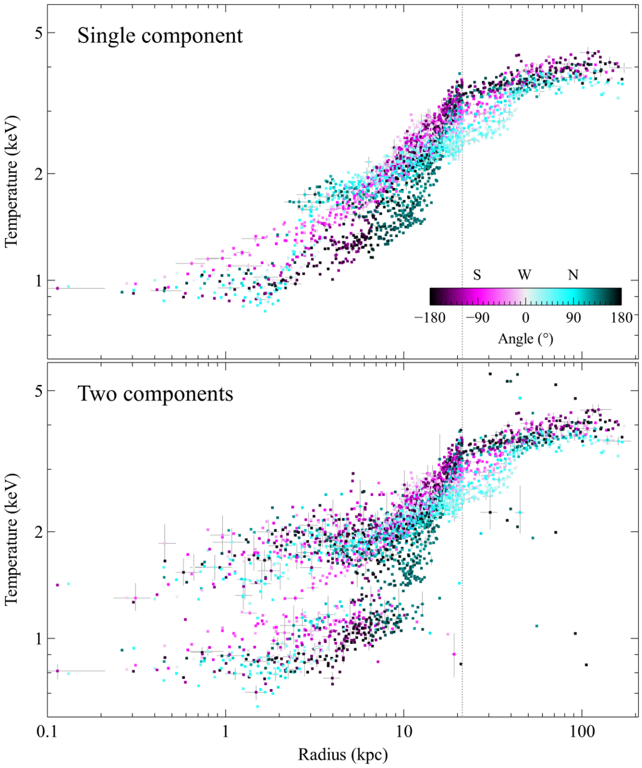

Figure B1. Radial profile of the temperatures in bins with a signal to noise ratio of 40 (inside the radius of ∼20 kpc marked by the dotted line) or 100 (outside that radius). The points are coloured according to their angle (angles are measured from the west, with positive values northwards). The radius is measured from the central radio source. The top panel shows a single-component fit to the spectra. The bottom panel shows the two temperatures for a two-component fit, if the temperatures of the two components can be constrained to better than 20 per cent, otherwise the single-component fit results are shown. Error bars are shown only for every 10th point.

unit cube of gas in the cluster, H, by its emissivity calculated using an APEC model. The enthalpy is $H = (5/2)\,\mathrm{k}Tn_{\mathrm{e,\,proj}}\,(1 + 1/X_{\mathrm{e/H}})$, where $X_{\mathrm{e/H}} \sim 1.2$ is the ratio of the number of electrons to hydrogen nuclei in a fully ionized plasma.

For the two-component fits, we assume that both components come from the same volume but they are in pressure equilibrium with each other. In this case, the electron density for component 1, in cm^{-3}, is given by

$$n_{\mathrm{e,proj,1}} = \left(\left[N_1 + N_2 \frac{T_2^2}{T_1^2} \right] \frac{4\pi D_{\mathrm{A}}^2 [1+z]^2}{10^{-14}\ V} X_{\mathrm{e/H}} \right)^{1/2}, \tag{B1}$$

where N_1 and N_2 are the XSPEC normalizations of the two components, respectively, T_1 and T_2 are the respective temperatures, V is the assumed volume (radius times area of bin on the sky, in cm^3) and D_{A} is the angular diameter of the source in cm and z its redshift. Monte Carlo realizations of the input data are used to derive the error bars in the computed quantities.

In Fig. B2, we examine the radial thermodynamic quantities computed from the two-component fits (showing the two-component result if both temperatures can be constrained, otherwise the single-component result). These plots show that there are distinct low-temperature branches in terms of density, cooling time and entropy, seen most easily in terms of cooling time. This material has high density, short cooling times and low entropy. This component appears to only be strong inside 12 kpc radius. If the two-component error threshold is increased, then additional points on these tracks are seen at larger radius, but not in great numbers.

These two branches are also seen in a plot of the temperature against density or pressure (Fig. B3). However, if the cooling time or entropy is plotted against the temperature, there appears to be a continuous distribution, although there may be a lack of values with temperatures around 1.3 keV.

When these projected values are compared to deprojected spectra (Fig. 23), we find reasonable agreement in some quantities, while others are offset. Projection effects appear to only weakly affect the temperature in Centaurus. Both the high- and low-temperature components are apparent in the deprojected results over the same radial range. The radius-as-depth assumption appears to overpredict the densities by a factor of 60 per cent at larger radius and 100 per cent in the centre. There is a similar overestimation of the pressure and underestimation of the cooling time and entropy.

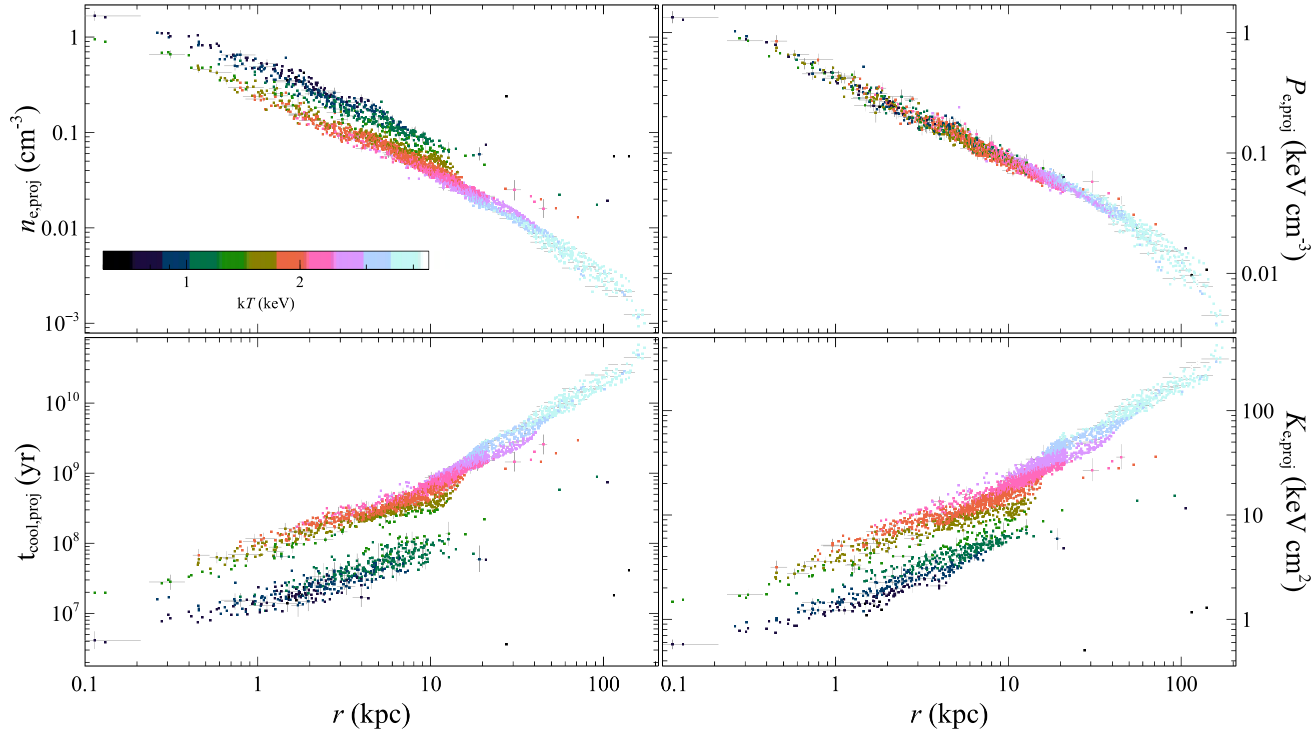

Figure B2. Radial plots of the projected electron density, electron entropy, electron pressure and mean radiative cooling time. The results are shown for two thermal components (with the number of components selected as in Fig. B1). Error bars are shown only for every 10th point. Points are coloured according to temperature. Note that for the pressure profile the assumption of pressure equilibrium forces the two-component results to have the same pressure.

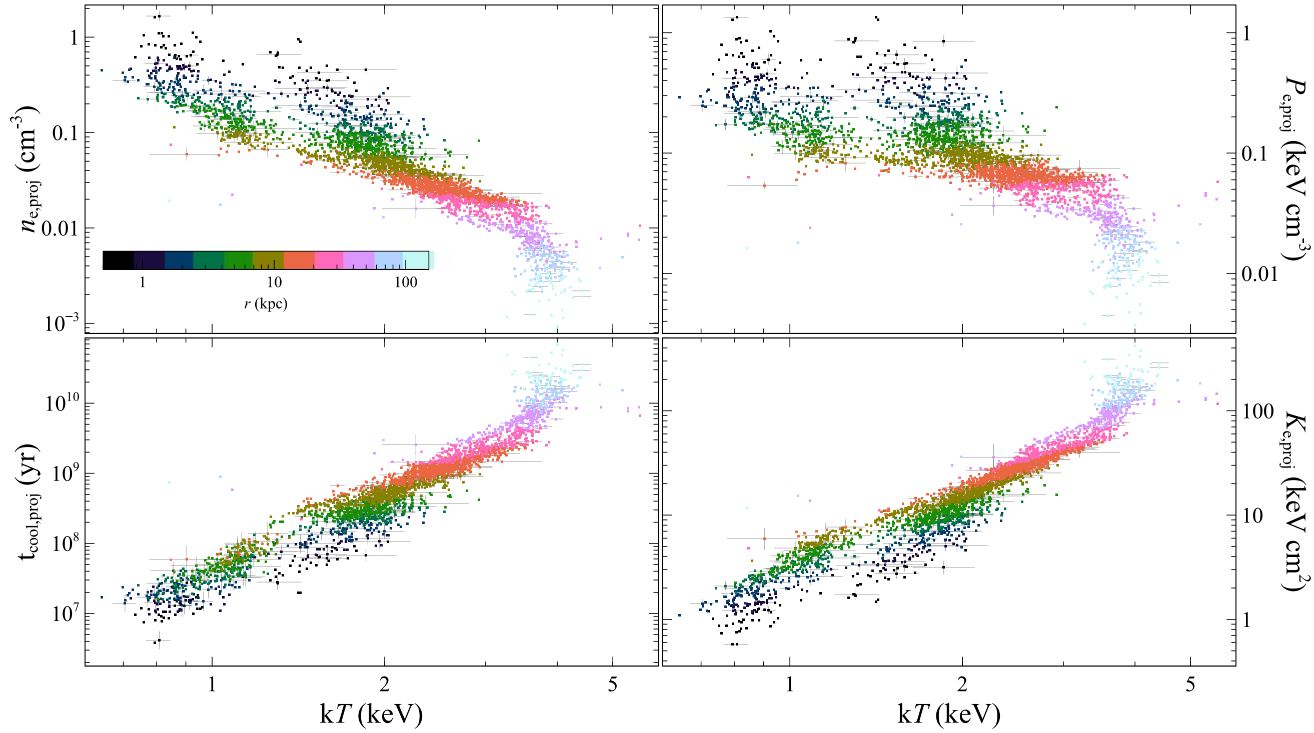

Figure B3. Plots of the two-component projected electron density, electron entropy, pressure and mean radiative cooling time as a function of temperature. Error bars are only shown for every 10th value. Points are coloured according to radius.

This paper has been typeset from a TEX/LATEX file prepared by the author.